

On using angular cross-correlations to determine source redshift distributions

Matthew McQuinn^{1,2} and Martin White^{1,2}

¹ *Department of Astronomy, University of California, Berkeley, CA 94720*

² *Department of Physics, University of California, Berkeley, CA 94720*

6 February 2013

ABSTRACT

We investigate how well the redshift distribution of a population of extragalactic objects can be reconstructed using angular cross-correlations with a sample whose redshifts are known. We derive the minimum variance quadratic estimator, which has simple analytic representations in very applicable limits and is significantly more sensitive than earlier proposed estimation procedures. This estimator is straightforward to apply to observations, it robustly finds the likelihood maximum, and it conveniently selects angular scales at which fluctuations are well approximated as independent between redshift bins and at which linear theory applies. We find that the linear bias times number of objects in a redshift bin generally can be constrained with cross-correlations to fractional error $\sqrt{10^2 N_{\text{bin}}/\mathcal{N}}$, where \mathcal{N} is the total number of spectra per dz and N_{bin} is the number of redshift bins spanned by the bulk of the unknown population. The error is often independent of the sky area and sampling fraction. Furthermore, we find that sub-percent measurements of the angular source density per unit redshift, dN/dz , are in principle possible, although cosmic magnification needs to be accounted for at fractional errors of $\lesssim 10$ per cent. We discuss how the sensitivity to dN/dz changes as a function of photometric and spectroscopic depth and how to optimize the survey strategy to constrain dN/dz . We also quantify how well cross-correlations of photometric redshift bins can be used to self-calibrate a photometric redshift sample. Simple formulae that can be quickly applied to gauge the utility of cross correlating different samples are given.

Key words: cosmology: theory – cosmology: large-scale structure

1 INTRODUCTION

In many spectral bands, the redshift distribution of a source population is difficult to determine (e.g., the radio, microwave, infrared, and X-ray). Even in the optical, where photometric techniques are widely applied to estimate source redshifts, these techniques work better for certain galaxy types than for others. However, extragalactic objects that are close together on the sky are also likely to be close in redshift. Thus, angular cross-correlations between populations with poorly known redshifts and those with better known redshifts can be used to improve the determination of the former's redshift distribution. Such reconstruction has a wide range of applications, from ascertaining the redshift distribution of diffuse backgrounds to calibrating photometric redshifts for the next generation of large-scale structure surveys.

Several previous studies have attempted to measure a population's redshift distribution, dN/dz , by using its con-

stituents' proximity on the sky to sources with known redshifts, i.e., by computing angular cross correlation statistics between the two populations (Phillipps & Shanks 1987; Erben et al. 2009). Similar techniques have been used to search for contamination in photometrically selected redshift slices or to bound the median redshift of a sample (Padmanabhan et al. 2007; Erben et al. 2009; Benjamin et al. 2010, 2012). Different dN/dz cross-correlation estimators have also been studied theoretically (Phillipps 1985; Newman 2008; Matthews & Newman 2010; Schulz 2010; Matthews & Newman 2012). However, it is unknown how close any of these estimators are to being optimal. It is also unclear which survey specifications (depth, area, sampling fraction, etc.) are best for reconstructing the redshift distribution of an unknown population.

This paper attempts to answer these questions. We write down the optimal dN/dz estimator and show that in very applicable limits, intuitive formulae describe how well the redshifts of a given source population can be con-

strained from a population whose redshift distribution is better known. In the limit of a dense spectroscopic survey, we show that the fractional error in the number of galaxies in the unknown population that fall in spectroscopic redshift bin z can be estimated to the precision

$$\frac{\delta N(z)}{N(z)} \sim 0.1 \left(\frac{\beta(z)}{0.1} \frac{f_{\text{sky}}}{10^{-3}} \right)^{-1/2} \left(\frac{\ell_0}{10^3} \right)^{-1}, \quad (1)$$

where f_{sky} is the sky coverage of the survey, ℓ_0 is the multipole at which shot noise becomes equal to intrinsic clustering in either sample, and $\beta(z)$ is the fraction of the unknown auto-power (at multipoles less than ℓ_0) that arises from redshift bin z . However, the result is even simpler in the limit of a sparse spectroscopic sample, having fewer than a thousand objects per sq. deg. per Δz :

$$\frac{\delta N(z)}{N(z)} \sim \left(\frac{\mathcal{N}^{(s)}}{10^3} \right)^{-1/2} \left(\frac{\beta(z)}{0.1} \right)^{-1/2}, \quad (2)$$

where $\mathcal{N}^{(s)}$ is the total number of spectra per unit redshift. In this ‘rare spectroscopic sample’ limit, the fractional error on $N(z)$ depends on the total number of spectra but *not* separately on the density of spectra, the sky area, or the fraction of objects with spectra.

Angular cross-correlations to determine redshifts have applications beyond estimating dN/dz . For example, they could be used to measure the redshifts of unresolved cosmic infrared background anisotropies (as was done in Kashlinsky et al. 2007) or to isolate foregrounds in cosmic microwave background (CMB) and high-redshift 21 cm maps. Angular cross-correlations can additionally be used to reconstruct three-dimensional correlations from angular clustering measurements (Seljak 1998; Padmanabhan et al. 2007). Furthermore, such cross-correlations are able to calibrate photometric redshift errors even when the spectroscopic population is not intrinsically identical to the unknown population. Applications that are not in the vein of precision cosmology likely need no better than a 10 per cent fractional constraint on dN/dz . However, percent-level or even better calibration of photometric redshifts is required to prevent redshift errors from being the limiting factor for cosmological parameter estimates with the next generation of weak lensing surveys (Huterer et al. 2006; Schneider et al. 2006; Bernstein & Huterer 2010; Zhang et al. 2010).¹

There are a wide range of surveys to which cross-correlation techniques could be applied. Recent spectroscopic surveys have gone wide over hundreds (Driver et al. 2011) or thousands of square degrees (Eisenstein et al. 2001; Colless et al. 2001; Drinkwater et al. 2010; SDSS-III Collaboration et al. 2012a) or deep over ~ 1 sq. deg. patches (Le Fèvre et al. 2005; Newman et al. 2012). Some are complete to a magnitude limit, whereas others more sparsely sample the sources (Lawrence et al. 1999; Eisenstein et al. 2001; Kochanek et al. 2012). The large spectroscopic data sets that should be available in the next decade include:²

- the Baryon Oscillation Spectroscopic Survey (BOSS) galaxy sample, covering $10,000 \text{ deg}^2$ with 1.5 million redshifts of massive galaxies extending to $z \simeq 0.7$ (Dawson et al. 2013),
- the Sloan Digital Sky Survey (SDSS)+BOSS quasar sample, covering $10,000 \text{ deg}^2$ with 2×10^5 redshifts (Schneider et al. 2010; Shen et al. 2011; SDSS-III Collaboration et al. 2012b),
- the Galaxy And Mass Assembly (GAMA) survey, covering 310 deg^2 with redshifts for 3.4×10^5 galaxies to a z -band magnitude limit of 19.8 (Driver et al. 2011),
- DEEP2 (Newman et al. 2012), the VIMOS-Very Large Telescope Deep Survey (VDSS; Le Fèvre et al. 2005), the z -Cosmology Evolution Survey (zCOSMOS; Lilly et al. 2007) and, while not technically spectroscopic, COMBO-17; (Wolf et al. 2003), each with $\sim 10^4 - 10^5$ redshifts in $\sim 1 \text{ deg}^2$ fields.
- the HETDEX survey gathering 10^6 Ly α emitting galaxies over 200 deg^2 at $1.8 < z < 3.8$ (Hill et al. 2008),
- 21cm emission line surveys over wide fields with e.g., the Australian Square Kilometer Array Pathfinder (ASKAP; Johnston et al. 2008), which aims for $\sim 10^6$ galaxies to $z \lesssim 0.43$ (Duffy et al. 2012).

The proposed projects eBOSS and BigBOSS would increase the number of spectroscopically identified galaxies and quasars by an order of magnitude over the existing SDSS + BOSS samples (Schlegel et al. 2011).³ Ultimately the Square Kilometer Array (projected for 2020) aims to capture a billion galaxies over half the sky (Rawlings et al. 2004).

In addition, we are entering a new age of optical photometric surveys, with the Kilo Degree Survey (KIDS; $1,500 \text{ deg}^2$ reaching an i -band magnitude limit of $i = 23$), the Dark Energy Survey (DES; $5,000 \text{ deg}^2$ to $i = 25$) and the HyperSuprimeCam Project (HSC; $2,000 \text{ deg}^2$ to $i = 26.2$) all currently gathering data. These surveys⁴ will be followed in the next decade by Large Synoptic Sky Telescope (LSST), which aims to constrain the cosmological model using a ‘gold sample’ of galaxies with $i < 25.3$ over half of the sky, and Euclid, which will provide high-resolution images of galaxies out to $z \sim 2$ over $15,000 \text{ deg}^2$. While we do not model in detail any particular survey, we use the above to guide our discussion.

Fig. 1 shows characteristic number densities with redshift for some of the aforementioned spectroscopic surveys as well as for complete surveys to the specified i band limiting magnitude. For these and ensuing calculations, we have parametrized the galaxy redshift probability distribution for

¹ While photometric redshifts are object-specific, in practice weak lensing studies will likely use the statistical distribution from photometric redshifts owing to catastrophic errors (Cunha et al. 2009; Mandelbaum et al. 2008). In contrast cross-correlations are not able to measure the redshifts of individual objects, but they are another way to measure this statistical distribution.

² <http://www.sdss.org>, <http://www.gama-survey.org>, <http://deep.ps.uci.edu>, <http://cesam.oamp.fr/vvdsproject/>, http://archive.eso.org/archive/adp/zCOSMOS/VIMOS_spectroscopy_v1.0/

³ <http://www.sdss3.org/future/eboss.php>, <http://bigboss.lbl.gov>

⁴ <http://kids.strw.leidenuniv.nl/>, <http://www.darkenergysurvey.org>, <http://www.naoj.org/Projects/HSC/HSCProject.html>, <http://www.lsst.org/lsst/>, <http://sci.esa.int/euclid>.

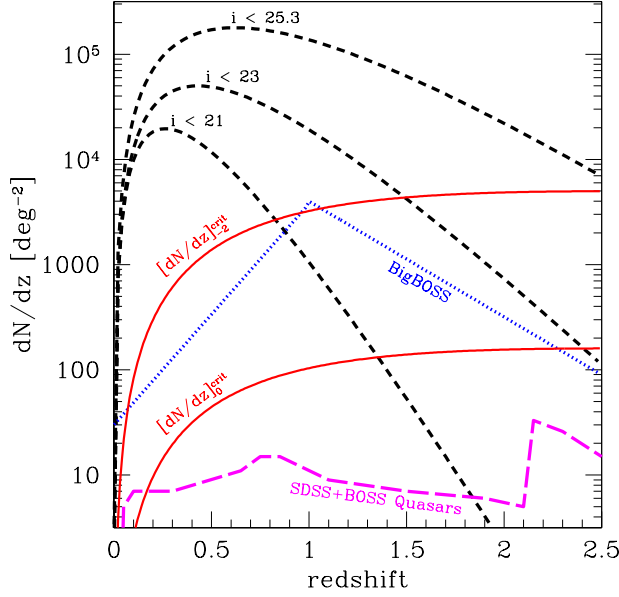


Figure 1. Shown are the dN/dz of different galaxy populations. The dashed curves are for surveys complete up to magnitude limits of $i = 21, 23$, and 25.3 , calculated via Eq. (3). Also shown are estimates for the density of SDSS+BOSS spectroscopic quasars and for the future combined density of luminous red galaxies, emission line galaxies, and quasars with BigBOSS. The red solid curves represent the critical densities for whether a sample is in the rare galaxy limit (Section 3.4).

an i -band magnitude limited sample as

$$p(z|i) = \frac{1}{2z_0} \left(\frac{z}{z_0} \right)^2 \exp \left[-\frac{z}{z_0} \right], \quad (3)$$

$$z_0 = 0.0417 i - 0.74,$$

with a total angular number density of $1.7 \times 10^{5+0.31(i-25)} \text{ deg}^{-2}$ (Hoekstra et al. 2006; LSST Science Collaboration et al. 2009, calibrated over the range $20.5 < i < 25.5$; see also Efstathiou et al. 1991; Brainerd et al. 1996; Benjamin et al. 2010; Hildebrandt et al. 2012).

Cross-correlation techniques can also be applied to maps in the X-ray such as those made with the X-ray Multi-Mirror Mission (XMM-Newton), in the ultraviolet such as with the Galaxy Evolution Explorer (GALEX), and in the infrared such as with the Wide field Infrared Survey Explorer (WISE) and the Herschel Space Observatory, the microwave such as with Atacama Cosmology Telescope (ACT) and the South Pole Telescope (SPT), and the radio such as with ASKAP.⁵ In many of these surveys, their angular resolution or depth makes redshift identification using overlapping optical surveys difficult. Cross-correlations offer an independent means to gauge redshifts.

This paper is organized as follows. Section 2 sets up the formalism used in this paper and applies it to an idealized dN/dz problem for illustration. Section 3 provides

intuition into the mechanics of the optimal estimator and discusses what scales contain the bulk of the information, setting the ground for the relevant examples discussed in Section 4. Section 5 generalizes our Fourier space results to configuration space and compares our estimator to the more familiar Newman (2008) estimator. Section 6 quantifies the estimator biases that result from common simplifying approximations. Penultimately, Section 7 shows how the results of the previous sections apply to photometric redshift calibrations. Finally, Section 8 demonstrates our estimator on mock surveys and is followed by our conclusions. We defer some technical details and derivations to a series of Appendices, which are referenced in the text. The numerical calculations in this study take a flat Λ CDM cosmological model with $\Omega_m = 0.27$, $\Omega_\Lambda = 0.73$, $h = 0.71$, $\sigma_8 = 0.82$, $n_s = 0.96$, and $\Omega_b = 0.046$, consistent with recent measurements (Larson et al. 2011). We treat the background cosmology as perfectly known in all calculations. Roman indexes $\{i, j, k\}$ run from 1 to some maximum integer whilst Greek indexes start from 0, and repeated indexes that do not appear in the same quantity are summed. Table 1 provides definitions of some commonly appearing symbols.

2 BASIC FORMALISM

We begin by introducing our notation and physical model, before deriving the most general form for our dN/dz estimator and applying it to idealized, illustrative examples. Useful limits of our expressions are taken in Section 3, where we also build intuition for the shape of the estimator.

2.1 Model and notation

Initially we will discuss galaxy clustering in the spherical harmonic basis as our covariance matrix is maximally sparse in this space. We shall write expressions as if the galaxy samples cover the full sky, but often finite sky coverage can be included by simply multiplying by the sky covering fraction (f_{sky}). Section 5.1 generalizes our estimation methods to configuration space, while Section 5.3 discusses the generalization to finite sky coverage.

We denote the multipole moments of a ‘photometric’ population of objects with unknown redshifts and a ‘spectroscopic’ sample in which the redshifts are perfectly known as

$$p(\ell, m) = N^{(p)} \delta^{(p)}(\ell, m) = \sum_{i=1}^{N_{\text{bin}}} N_i^{(p)} \delta_i^{(p)}(\ell, m), \quad (4)$$

$$s_i(\ell, m) = N_i^{(s)} \delta_i^{(s)}(\ell, m), \quad (5)$$

respectively. Here, $1 \leq i \leq N_{\text{bin}}$ labels the redshift bin spanning the range $z_{i-1} - z_i$, where the z_i are ordered in increasing redshift, and $\delta^{(x)} \equiv x/\langle x \rangle - 1$ is the overdensity in population x , where x denotes an angular source density field with $\langle x \rangle = N^{(x)}$, the mean density per unit area. Our calculations are more general than the case of a spectroscopic and photometric galaxy sample: the photometric sample can be thought of as any sample for which the redshifts are unknown and the spectroscopic as one for which they are known to precision $\Delta z/2$. Our ultimate aim is to

⁵ <http://xmm.esac.esa.int>, <http://www.galex.caltech.edu>, <http://wise.ssl.berkeley.edu>, sci.esa.int/herschel/, <http://www.princeton.edu/act/>, <http://pole.uchicago.edu>, <http://www.atnf.csiro.au/projects/mira/>

symbol	description
$p(\ell, m)$	multipole moment of photometric population (subscript i refers to the subsample within redshift bin i)
$\mathbf{s}(\ell, m)$	vector of multipole moments of spectroscopic z -bins (s_i is component in bin i)
$N_i^{(x)}$	average density per unit area in population x in redshift bin i ; $N^{(x)} \equiv \sum_{i=1}^{N_{\text{bin}}} N_i^{(x)}$
$dN_i^{(x)}/dz$	equal to $N_i^{(x)}/\Delta z_i$, where the subscript i is dropped if redshift-independent
$N_i^{(s)}$	total number of spectroscopic galaxies per unit redshift in redshift bin i
$w^{(xy)}(\ell)$	stochastic component of the cross power between samples x and y ; $w^{(x)} \equiv w^{(xx)}$
$b_i^{(x)}$	linear bias of population x in redshift bin i
$C_{ij}(\ell)$	matter density angular cross power spectrum between bins i and j
$\mathbf{A}(\ell, m)$	covariance matrix of $p(\ell)$ with $\mathbf{s}(\ell)$ with index 0 referring to p
ℓ_0	multipole where shot noise is equal to cosmic variance
N_{bin}	number of redshift bins used in analysis
$D(z)$	growth factor such that $D(0) = 1$; $D_i \equiv D(z_i)$
χ	the conformal distance; $d\chi = (1+z)dt$
$S(\ell)$	the ‘Schur parameter’ (Eq. 29); $S \geq 1$, with equality holding in the rare limit
$\beta_i(\ell)$	fraction of total photometric power contributed by redshift bin i (Eq. 43)
n	local power-law index of the density power spectrum such that $P(k) \sim k^n$
ℓ_{NL}	multipole at which linear theory errors at a factor of 2 (Eq. 34)

Table 1. Definitions of commonly appearing symbols. The arguments are often dropped in the text, and hats on any symbol indicates an estimated value.

use a survey’s estimates for the left-hand-side of Eqs. (4) and (5), $\hat{p}(\ell, m)$ and $\hat{s}_i(\ell, m)$, to estimate the $N_i^{(p)}$.

Our discussion will be couched in terms of constraining the $N_i^{(p)}$ for which the Δz_i need to be chosen to be sufficiently narrow in order that there are not significant gradients in $dN^{(p)}/dz$ across the bin. However, in many cases, particularly when the sensitivity to cross correlations is marginal, a smoother parametrization of $dN^{(p)}/dz$ may be desirable. Our error estimates can be easily translated into the errors on other parameterizations of $dN^{(p)}/dz$ (like its mean and variance or the empirically motivated parameterization of a power-law times an exponential; see Appendix A3 for more details).

We model the $s_i(\ell, m)$ as Gaussian random variables with auto power spectrum

$$\langle s_i s_j \rangle(\ell) = N_i^{(s)} N_j^{(s)} b_i^{(s)} b_j^{(s)} C_{ij}(\ell) + w_i^{(s)} \delta_{ij}^K, \quad (6)$$

where we have dropped the m dependence as different modes are orthogonal by statistical isotropy but have the same auto-power. We denote by C_{ij} the cross power between the matter overdensity in the i and j slices, and by $b_i^{(x)}$ the linear bias of population x in redshift bin i . The expression for the shot noise piece $w_i^{(s)}$ in the halo model results from taking the large-scale limit of the one-halo term (see e.g. Cooray & Sheth 2002, for a review):

$$w_i^{(xy)} = \int_{\chi_{i-1}}^{\chi_i} d\chi \int dm_h n_h(m_h) \langle n_g^{(x)} n_g^{(y)} | m_h \rangle, \quad (7)$$

where $n_h(m_h)$ is the halo mass function and $\langle n_g^{(x)} n_g^{(y)} | m_h \rangle$ is the number of galaxies of type x in a halo of mass m times that in type y and averaged over all haloes at fixed mass.⁶ This large-scale limit is a good approximation at the angular scales we consider. We adopt the simplifying notation $w_i^{(x)} \equiv w_i^{(xx)}$. We note that a measurement of the $N_i^{(p)}$ is not limited

by sample variance, and it can be perfectly measured in the limit that the stochastic component is zero.

The cross power spectrum of $s_i(\ell)$ and $p(\ell)$ is

$$\langle p s_i \rangle(\ell) = N_i^{(s)} b_i^{(s)} \sum_{j=1}^{N_{\text{bin}}} N_j^{(p)} b_j^{(p)} C_{ij}(\ell) + w_i^{(ps)}. \quad (8)$$

Finally,⁷

$$\langle p^2 \rangle(\ell) = \sum_{i=1}^{N_{\text{bin}}} \sum_{j=1}^{N_{\text{bin}}} \left[N_i^{(p)} b_i^{(p)} N_j^{(p)} b_j^{(p)} C_{ij}(\ell) + w_i^{(p)} \delta_{ij}^K \right]. \quad (9)$$

We will add to Eqs. (6), (8) and (9) the generally smaller terms that owe to cosmic magnification later.

While our formalism is completely general, subsequent calculations (and the figures we present) assume

$$b_i^{(x)} = D(z_i)^{-1}, \quad (10)$$

where $D(z)$ is the linear growth factor normalized so that $D(0) = 1$, and we will interchangeably use χ and z for its argument. This bias leads to redshift-independent clustering, appropriate for several cosmological populations, especially if they are rare objects. In many instances this assumption will be benign, and our results can be simply rescaled by fixing $N_i^{(x)} b_i^{(x)}$. We also assume

$$w_i^{(x)} = \left(\frac{1 + 3 f_{\text{sat}}^{(x)}}{1 + f_{\text{sat}}^{(x)}} \right) N_i^{(x)}, \quad (11)$$

$$w_i^{(ps)} = f_{\text{over}} \min[w_i^{(s)}, w_i^{(p)}], \quad (12)$$

for the stochastic component of the power. We take the ‘overlap fraction’ to be $f_{\text{over}} = 1$ unless stated otherwise (which means that the rarest $\min[N_i^{(s)}, N_i^{(p)}]$ sources are the same in both samples). In addition, we take a satellite fraction of $f_{\text{sat}}^{(x)} = 0$. Increasing $f_{\text{sat}}^{(x)}$ to 25 per cent – the

⁶ The normalization of the stochastic component can potentially be reduced for dense samples by differently weighting sources (Seljak et al. 2009; Hamaus et al. 2010) instead of the galaxy number weighting used here.

⁷ The total linear bias of the photometric sample is $b^{(p)} = \sum_{i=1}^{N_{\text{bin}}} N_i^{(p)} b_i^{(p)} / N^{(p)}$, which provides a potentially helpful integral constrain to break the $b_i^{(p)} - N_i^{(p)}$ degeneracy.

largest fraction found for the relevant galaxies in Wetzel & White (2010, see their figs. 8 & 12) – does not change our results appreciably.⁸

The cross power in the matter overdensity is

$$C_{ij}(\ell) = \int_0^\infty \frac{2k^2 dk}{\pi} \alpha_\ell(k, z_i) \alpha_\ell(k, z_j) P(k), \quad (13)$$

$$\alpha_\ell(k, z_i) = \int_0^\infty d\chi D(\chi) W_i(\chi) j_\ell(k\chi), \quad (14)$$

where, in our top hat $N_i^{(p)}$ bias, $W_i = \Delta\chi_i^{-1}$ for redshifts that fall in the range $z_{i-1} - z_i$ and zero otherwise. (For a discussion of how to evaluate j_ℓ and these highly-oscillatory integrals over j_ℓ numerically see Appendix D.) While not required, we have assumed linear theory such that $P(k)$ is the $z = 0$ linear-theory matter overdensity power spectrum. Eq. (13) ignores redshift space distortions (RSDs). RSDs contribute a small fraction to the angular fluctuations on relevant angular scales (Appendix B).

We note that linear scales can only be used to reconstruct the *product* of the large-scale bias, $b_i^{(p)}$, and the number density, $N_i^{(p)}$, at any redshift (Newman 2008; Bernstein & Huterer 2010; Schulz 2010) as they always appear in combination. This product is sometimes the desired quantity (e.g., when cleaning a map of diffuse backgrounds), but for many applications it is $N_i^{(p)}$ itself that is desired. We discuss methods for breaking this degeneracy in Section 9. *We will often write our constraints as on $N_i^{(p)}$ for notational simplicity, but please note that the constraints we quote are always on the combination $b_i^{(p)} N_i^{(p)}$.*

2.2 Estimator

To simplify notation, we define the combined covariance matrix of the photometric survey and the redshift slices of the spectroscopic survey:

$$\mathbf{A}(\ell, m) \equiv \left\langle \begin{pmatrix} \hat{p}(\ell, m)^* \\ \hat{s}(\ell, m)^* \end{pmatrix} \begin{pmatrix} \hat{p}(\ell, m) & \hat{s}(\ell, m) \end{pmatrix} \right\rangle, \quad (15)$$

where $\hat{\mathbf{s}}^T = (\hat{s}_1, \dots, \hat{s}_n)$. The argument (ℓ, m) will typically be dropped in subsequent expressions. The minimum variance estimator for $N_i^{(p)}$ that maximizes the likelihood function if it is Gaussian in this parameter near the maximum (as is likely if many modes are included in the estimate) is

$$\begin{aligned} \hat{N}_i^{(p)} &= [\hat{N}_i^{(p)}]_{\text{last}} + \frac{1}{2} [\mathbf{F}^{-1}]_{ij} \sum_{\ell, m} \left[\begin{pmatrix} \hat{p} & \hat{s} \end{pmatrix} \mathbf{Q}_j \begin{pmatrix} \hat{p} \\ \hat{s} \end{pmatrix} \right. \\ &\quad \left. - \text{Tr}[\mathbf{A}^{-1} \mathbf{A}_{,j}] \right], \end{aligned} \quad (16)$$

$$\mathbf{Q}_j \equiv \sum_{\ell, m} \mathbf{A}^{-1} \mathbf{A}_{,j} \mathbf{A}^{-1}, \quad (17)$$

(e.g. Bond et al. 1998; Tegmark et al. 1998; Dodelson 2003), where all repeated indexes are summed and subscript ‘ i ’ indicates a derivative with respect to the i^{th} parameter, which for most of our discussion is the parameter $N_i^{(p)}$. One can

also trivially recast this to $b_i^{(p)} N_i^{(p)}$, the quantity that is truly constrained. Appendix A2 derives Eqs. (16) and (17) and shows how they generalize to the case with priors on the $N_i^{(p)}$. The parameter $[\hat{N}_i^{(p)}]_{\text{last}}$ is initially a guess and, for subsequent iterations, the previous estimate. In the limit that many modes are included in the estimate (which is appropriate; Appendix A1),

$$F_{ij} = \frac{1}{2} \sum_{\ell, m} \text{Tr} [\mathbf{A}^{-1} \mathbf{A}_{,i} \mathbf{A}^{-1} \mathbf{A}_{,j}], \quad (18)$$

and \mathbf{F} is the Fisher matrix. The estimator in this limit is the minimum variance quadratic estimator, and the variance of this estimator is $[\mathbf{F}^{-1}]_{ii}$ (e.g., Tegmark et al. 1997). We will use Eq. (18) in our subsequent calculations.

Schulz (2010) and Matthews & Newman (2012) considered a maximum likelihood estimator approach to constrain the $N_i^{(p)}$, at least for their most general expressions. This approach should yield similar estimates to ours as the Fisher matrix, which sets our variance, saturates the Rao-Cramer bound (and so is optimal). In fact, quadratic estimators are prone to find local extrema and so a Markov Chain Monte Carlo approach to find the maximum likelihood may yield more robust estimates (e.g., Christensen et al. 2001). However, the linearity of our estimator reduces the severity of this problem, and we show in Section 8 that it robustly finds the true minimum even when the initial guess for the $N_i^{(p)}$ is off by orders of magnitude.

It is worth noting two subtleties in our approach: First, we do not consider estimators for the $N_i^{(p)}$ that simultaneously estimate the $w_i^{(ps)}$, although this would be a small generalization of Eq. (16). Instead, we assume that the $w_i^{(ps)}$ can be measured independently from the $N_i^{(p)}$, which should hold because of the much different scaling of the cosmological and stochastic components in the $\langle p s_i \rangle$. Larger ℓ can also be utilized for the $w_i^{(ps)}$ estimate than are useful for constraining the $N_i^{(p)}$. Second, our expressions do not consider the case in which the true value for $N_i^{(s)}$ differs from the measured number density owing to large-scale modes on the scale of the survey. Such an error will be most important in narrow fields. One can easily take this effect into account by using the measured number in a prior on the field to field fluctuations and then marginalizing over the $N_i^{(s)}$ (Appendix A2).

2.3 Idealized application

Bearing these caveats in mind, Eq. (18) allows us to estimate the sensitivity of a hypothetical survey. The solid curves in Fig. 2 show these estimates for an idealized case in which the $N_i^{(x)}$ are equal, have redshift-independent clustering (see Eq. 10), and span the redshift range 0 – 1 with 10 redshift bins. The curves represent contours of constant sensitivity on the parameter $b_{\text{bin}/2}^{(p)} N_{\text{bin}/2}^{(p)}$ (i.e., the fractional error on the bias times the angular number density of photometric objects in the fifth redshift bin) as a function of the $dN^{(p)}/dz$ and $dN^{(s)}/dz$ used in the cross correlations. The labels on the black solid curves are \log_{10} of the fractional error. The solid curves in the right panel of Fig. 3 are the same except assuming a survey in which $z = 0 - 1$ is spanned with 100 redshift bins, which approximately results in $\sqrt{10}$

⁸ In the case of $f_{\text{over}} = 1$ and equal numbers in both the s and p samples, both populations trace the same large-scale cosmological plus stochastic perturbations and the $N_i^{(p)}$ can be perfectly estimated.

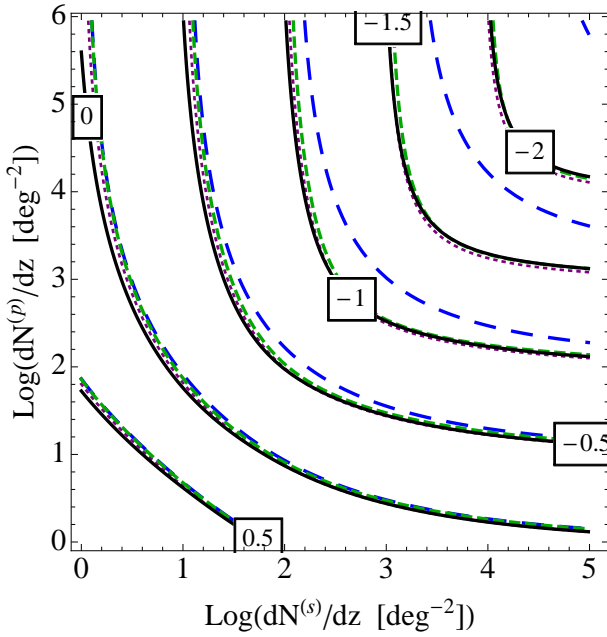


Figure 2. Contours of \log_{10} of the fractional error in $b_{\text{bin}/2}^{(p)} N_{\text{bin}/2}^{(p)}$ for an idealized survey where the $N_i^{(x)}$ are equal and span $z = 0-1$ with 10 redshift bins of equal width, covering 1 per cent of the sky (400 deg^2). Contours are labelled for the solid curves, and the corresponding contour for the other curves is the adjacent curve at higher number densities. The calculations assume our fiducial parameters except $f_{\text{over}} = 0$. (For our fiducial value of $f_{\text{over}} = 1$, the curves buckle outward when the number densities become equal.) The black solid curves are the full calculation (in the Limber approximation, but this matters negligibly for $\Delta z \approx 0.1$). The purple dotted curves show the approximation that sets to zero terms in \mathbf{F} in which the derivatives hit A_{00} . The short dashed green is the diagonal approximation to the remaining Fisher matrix, a limit that also works excellently. The long dashed blue is the error on the estimator in the Schur-Limber limit in which $S \rightarrow 1$ (Section 3.2 and Eq. 35).

larger errors. The other contours in both figures show different approximations that are developed in Section 3. All of the curves are computed for a fractional sky coverage of $f_{\text{sky}} = 0.01$, but the errors scale as $f_{\text{sky}}^{-1/2}$ for surveys with areas $\gg 1 \text{ deg}^2$ (Section 5.3).

While the contours in Figs. 2 and 3 are for the simplistic case of constant $dN^{(p)}/dz$ and $dN^{(s)}/dz$, they illustrate a few of our results. First, the sensitivity to the $N_i^{(p)}$ saturates once either the photometric or spectroscopic dN/dz becomes larger than the other. Second, the contours show that percent-level constraints for $\Delta z = 0.1$ are possible even for number densities of $dN^{(s)}/dz \sim dN^{(p)}/dz \sim 10^3 \text{ deg}^{-2}$ if 10 per cent of the sky is utilized.

We find that the calculations in Figs. 2 and 3 can be crudely applied beyond the assumption of constant $dN^{(p)}/dz$, of constant $dN^{(s)}/dz$, or of the redshift at which they were computed. For example, if these calculations are used to estimate the sensitivity of the LSST gold sample, which will have $dN^{(p)}/dz \sim 10^5 \text{ deg}^{-2}$ over a quarter of the sky (LSST Science Collaboration et al. 2009), one finds that percent-level determinations of the $N_i^{(p)}$ are possible in $\Delta z \sim 0.1$ bins with spectroscopic follow up of

$dN^{(s)}/dz \sim 10^3 \text{ deg}^{-2}$ (comparable to the sky density of BigBOSS emission line galaxies). This estimate is consistent with the conclusions of more detailed calculations (Section 4). Also, the LEGACY plus the ongoing BOSS quasar samples on SDSS provide a spectroscopic number density of $dN^{(s)}/dz \sim 10 \text{ deg}^{-2}$ out to $z \approx 2.7$ over $\sim 10^4 \text{ deg}^{-2}$ (with double this number density at $z \sim 2.3$; SDSS-III Collaboration et al. 2012b). Fig. 2 suggests that cross-correlations with denser photometric surveys should provide ~ 10 per cent errors on their $N_i^{(p)}$ for $f_{\text{sky}} \sim 0.1$, again consistent with what we find later on.

We now turn to building intuition for the estimator presented in Section 2.2.

3 APPROXIMATIONS AND SPECIAL CASES

In this section, we provide an understanding of the shape of the contours in Figs. 2 and 3, we discuss which scales contribute the $N_i^{(p)}$ estimate, and we provide intuitive formulae that can be quickly applied to gauge the utility of cross correlating different samples.

3.1 The Limber approximation

If the theoretical power spectrum is smooth and our signal is coming primarily from scales which are small compared to the width of each redshift shell, then the Limber approximation applies (Limber 1953, 1954) and our expressions simplify significantly. The Limber approximation assumes that $P(\mathbf{k}_\perp, k_\parallel)$ varies slowly as a function of k_\parallel compared to $j_\ell(k_\parallel \chi)$ – which should hold when $\ell \gg \chi/\Delta\chi_i$. Making use of the identity

$$\int k^2 dk j_\ell(k\chi) j_\ell(k\chi') = \frac{\pi}{2\chi^2} \delta^D(\chi - \chi'), \quad (19)$$

where δ^D is the Dirac delta function and the Limber approximation, Eq. (13) simplifies dramatically and $C_{ij}(\ell)$ becomes diagonal (Kaiser 1992; White & Hu 2000)

$$C_{ij}(\ell) = \delta_{ij}^K \int_0^\infty d\chi D^2(\chi) W_i^2(\chi) \frac{P(\ell/\chi)}{\chi^2}, \quad (20)$$

$$\approx \delta_{ij}^K D^2(z_i) \frac{P(\ell/\chi)}{\chi^2 \Delta\chi_i}. \quad (21)$$

We discuss how the Limber limit is approached and compute the corrections owing to RSDs in Appendix B (where we show that RSDs enter at $\mathcal{O}([\ell \Delta\chi/\chi]^{-2})$, which means they contribute negligibly on scales where the Limber approximation applies).

The majority of past studies (Newman 2008; Matthews & Newman 2010; Schneider et al. 2006) have used the Limber approximation. Fig. 3 shows that this approximation provides a good estimate for the variance of our $N_i^{(p)}$ estimator, with only a small error in the case of $\Delta z = 0.1$ (left panel) and the error starting to become significant for $\Delta z = 0.01$ (right panel). In both panels, compare the solid contours, which assume Limber, with the dashed contours, which do not. The Limber approximation is accurate because, as we will show, much of the estimator’s constraint derives from ℓ where it should hold. (The percent-level bias introduced by this approximation is quantified in Section 6.)

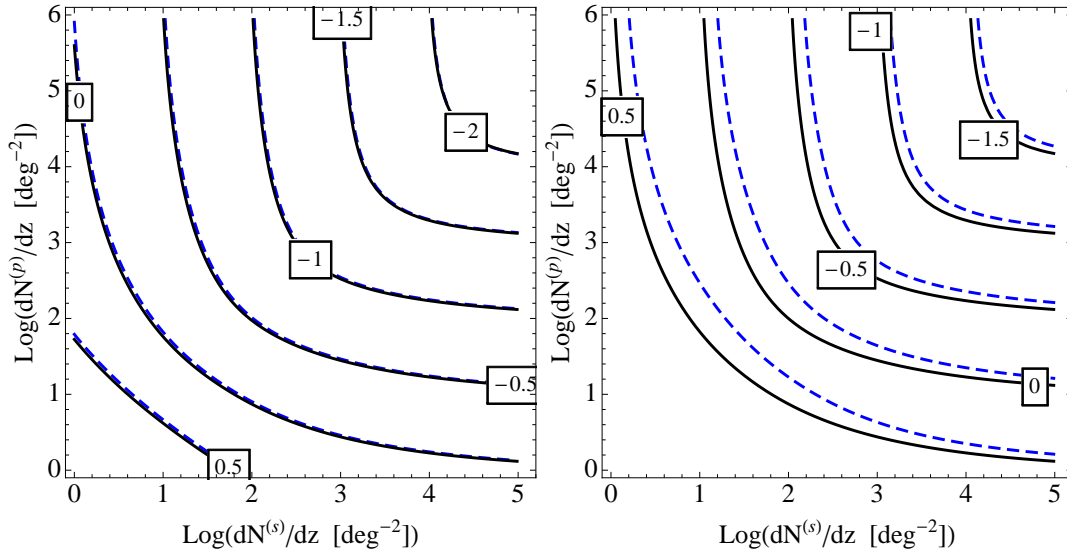


Figure 3. Contours of \log_{10} of the fractional error in $b_{\text{bin}/2}^{(p)} N_{\text{bin}/2}^{(p)}$ in the Limber approximation (black solid curves) and the full calculation without this approximation (blue dashed curves; which for the same fractional error fall immediately upward of the solid curves). The contours are calculated for a survey that spans $z = 0 - 1$ with 10 (left panel) and 100 (right panel) redshift bins of equal width over 1 per cent of the sky. Roughly, the errors are $\sqrt{10}$ larger in the right panel than in the left panel. This figure illustrates that the Limber approximation works well for the $\Delta z = 0.1$ case, but is starting to break down at $\Delta z = 0.01$. While making the Limber approximation leads to errors in the uncertainty estimate, we show in Section 6 that the bias on $N_i^{(p)}$ is always quite small.

The covariance matrix of the photometric and spectroscopic surveys simplifies considerably in the Limber approximation, with only the $A_{0\alpha}$ terms and the diagonal components of A_{ij} being nonzero, namely

$$A_{00} = \sum_{i=1}^{N_{\text{bin}}} \left(b_i^{(p)} N_i^{(p)} \right)^2 C_{ii} + w_i^{(p)}, \quad (22)$$

$$A_{0i} = b_i^{(p)} N_i^{(p)} b_i^{(s)} N_i^{(s)} C_{ii} + w_i^{(ps)}, \quad (23)$$

$$A_{ij} = \delta_{ij}^K \left[\left(b_i^{(s)} N_i^{(s)} \right)^2 C_{ii} + w_i^{(s)} \right], \quad (24)$$

$$[A_{0i}]_{,i} = b_i^{(p)} b_i^{(s)} N_i^{(s)} C_{ii}. \quad (25)$$

Furthermore, this $\mathbf{A}(\ell, m)$ can be inverted analytically, yielding

$$[\mathbf{A}^{-1}]_{00} = \frac{S}{A_{00}}, \quad (26)$$

$$[\mathbf{A}^{-1}]_{0i} = -\frac{S}{A_{00}} \frac{A_{0i}}{A_{ii}} = -\frac{S r_i^2}{A_{0i}}, \quad (27)$$

$$[\mathbf{A}^{-1}]_{ij} = \frac{\delta_{ij}^K}{A_{ii}} + \frac{S}{A_{00}} \frac{A_{0i} A_{0j}}{A_{ii} A_{jj}} = \frac{\delta_{ij}^K}{A_{ii}} + S \sqrt{\frac{r_i^2 r_j^2}{A_{ii} A_{jj}}}, \quad (28)$$

with

$$S = A_{00} \left(A_{00} - \sum_{i=1}^{N_{\text{bin}}} \frac{A_{0i}^2}{A_{ii}} \right)^{-1} = \left(1 - \sum_{i=1}^{N_{\text{bin}}} r_i^2 \right)^{-1}, \quad (29)$$

where $r_i(\ell) \equiv A_{0i}/(A_{00} A_{ii})^{1/2}$ is the cross correlation coefficient between p and s_i , and again we are using the convention $i, j \in 1 - N_{\text{bin}}$. The above inverse can be derived using the Schur complement matrix identity and the Sherman-Morison Woodbury formula (Petersen & Pedersen 2008, their equations 8.8.3 and 3.2.1).

The ‘Schur parameter’, S , is greater than or equal to unity and quantifies the extent of correlation between the

spectroscopic and photometric samples. In the case of complete redshift overlap of the spectroscopic sample and in the absence of shot-noise, $S \rightarrow \infty$ and the $N_i^{(p)}$ are perfectly constrained. If the unknown sample is limited by shot-noise, or if the two samples cover different redshift ranges, $S \rightarrow 1^+$. The implication is that even a small amount of noise diminishes considerably the constraining power of a mode.

In the analytic derivations that follow, we ignore derivatives that hit the A_{00} in Eqs. (16) and (18), as this element provides only an integral-like constraint on the $N_i^{(p)}$. For all relevant limits, the approximation of ignoring the A_{00} -derivatives is excellent: Fig. 2 compares the solid black error contours, which include the A_{00} -derivatives, with the nearly-overlapping dotted purple contours, which do not. With this additional simplification, the Limber-approximation Fisher matrix (Eq. 18) is

$$\begin{aligned} F_{ij} &\approx \sum_{\ell, m} \left([\mathbf{A}^{-1}]_{ij} [\mathbf{A}^{-1}]_{00} + [\mathbf{A}^{-1}]_{0i} [\mathbf{A}^{-1}]_{0j} \right) [A_{0i}]_{,i} [A_{0j}]_{,j}, \\ &= \sum_{\ell, m} \frac{S}{A_{00}} \left(\frac{\delta_{ij}^K}{A_{ii}} + 2 S \sqrt{\frac{r_i^2 r_j^2}{A_{ii} A_{jj}}} \right) [A_{0i}]_{,i} [A_{0j}]_{,j}. \end{aligned} \quad (30)$$

Furthermore, the minimum variance quadratic estimator becomes

$$\begin{aligned} \hat{N}_k^{(p)} &= [\hat{N}_k^{(p)}]_{\text{last}} + [\mathbf{F}^{-1}]_{ki} \sum_{\ell, m} \frac{S [A_{0i}]_{,i}}{A_{00} A_{ii}} \\ &\times \left\{ \left(\delta_{ij}^K + 2 S \sqrt{\frac{r_i^2 r_j^2}{A_{jj}}} \right) \hat{p}_j \hat{s}_j - A_{0i} \right\}, \end{aligned} \quad (31)$$

where repeated indices that do not appear in same quantity

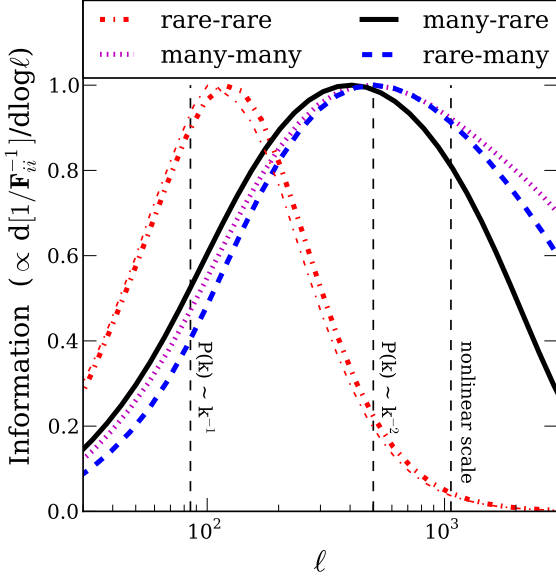


Figure 4. An illustration of the scales that contribute to the constraint on $N_i^{(p)}$ in different limits. The areas under these curves, which are of $d[1/\mathbf{F}_{ii}^{-1}]/d\log\ell$, are proportional to the information that contributes to the estimate in the $i = 6$ bin for a measurement in 10 redshift bins with $\Delta z = 0.1$ and spanning $0 < z < 1$. For illustrative purposes we have assumed constant $dN^{(p)}/dz$ and $dN^{(s)}/dz$. The first adjective for each curve’s label in the key describes the spectroscopic sample (rare= 10 deg^{-2} and many= 10^5 deg^{-2}), and the second describes the photometric sample (rare= 100 deg^{-2} and many= 10^6 deg^{-2}). However, the curves are not significantly impacted at linear scales by the assumed densities as long as ‘many’ equates to $\gtrsim 10^4 \text{ deg}^{-2}$ and ‘rare’ to $\lesssim 10^3 \text{ deg}^{-2}$, with the exception being the many-many case. In the text we describe why these limits select the scales that they do. The vertical lines denote significant scales discussed in the text. The thin red dot-dashed curve does not assume the Limber approximation whereas the corresponding thick curve assumes it.

are summed. (The complete Limber estimator, where $[A_{00}]_i$ terms are maintained, is given in Appendix A1.)⁹

Figs. 4, 5 and 6 motivate why the approximations of Limber and linear theory are justified. Fig. 4 shows the scales that contribute to the estimator for several different cases, plotting $d[1/\mathbf{F}_{ii}^{-1}]/d\log\ell$. The areas under these curves are proportional to the information that contributes to the estimate in the $i = 6$ bin for a measurement in 10 redshift bins with $\Delta z = 0.1$ spanning $0 < z < 1$. The first adjective for each curve’s label in the key describes the spectroscopic sample (rare= 10 deg^{-2} per dz and many= 10^5 deg^{-2} per dz) and the second describes the photometric sample (rare= 100 deg^{-2} per dz and many= 10^6 deg^{-2} per dz), where these number densities are assumed constant with redshift for illustration. This figure indicates that (at least for these

⁹ Our Limber “Fisher Matrix” that drops the off-diagonal terms can violate the Rao-Cramer bound, as can be noted in Fig. 2: The purple dotted contours are not above the black solid contours (which saturate the Rao-Cramer bound for our problem) at all number densities, falling just slightly below at the largest $dN^{(s)}/dz$. This is not an issue for our purposes.

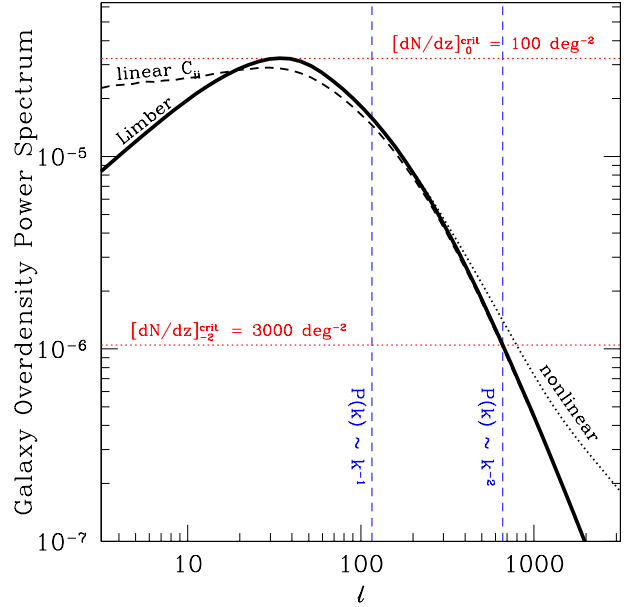


Figure 5. Shown are C_{ii} for $z_i = 1$, $\Delta z_i = 0.1$, and our fiducial bias model. The C_{ii} are calculated under various approximations – linear theory (dashed curve) and the Limber approximation (solid curves) – and for the full Peacock & Dodds (1996) nonlinear power spectrum (dotted curve). Also depicted are the stochastic component of the power for two characteristic number densities and $f_{\text{sat}} = 0$ (horizontal lines). The auto-power of spectroscopic bin i , $\langle s_i^2 \rangle$, equals C_{ii} plus the stochastic component. The optimal quadratic estimator selects information that roughly falls in the range of the two vertical lines (Section 3), between where the $P(k)$ roughly scales as k^{-1} and k^{-2} . Conveniently, both linear theory and the Limber approximation apply around these scales.

extremities of the parameter space) the bulk of the information derives from modes around where the density power spectrum has power-law index -2 and -1 , ℓ_{Pk-2} and ℓ_{Pk-1} , respectively. As we shall discuss further, correlations between two rare samples (where rare is defined as having $\ell_0 \lesssim \ell_{Pk-1}$) constrain $N_i^{(p)}$ primarily from multipoles with $\ell \sim \ell_{Pk-1}$. Rare and abundant samples use multipoles with $\ell \sim \ell_{Pk-2}$, which also holds in the case in which both samples are extremely abundant. We show later that it is possible in less extreme examples in which both samples are relatively abundant for the information to derive primarily from the scale ℓ_0 .

To orient the reader, Fig. 5 shows estimates for the C_{ii} at $z = 1$ and for $\Delta z = 0.1$ that use linear theory, the Limber approximation, and the Peacock & Dodds (1996) nonlinear power spectrum. The vertical lines show ℓ_{Pk-2} and ℓ_{Pk-1} . ℓ_0 is the scale at which the (horizontal) stochastic power becomes equal to the C_{ii} , i.e. where the dotted (red) lines equal the black curve. We show the stochastic terms for two illustrative number densities. In particular, the upper horizontal line in Fig. 5 is the lowest number density at which $w_i^{(s)} > [b_i^{(s)} N_i^{(s)}]^2 C_{ii}$ is satisfied at *all* ℓ , which we denote as $[dN/dz]_0^{\text{crit}}$, where

$$\left[\frac{dN}{dz} \right]_0^{\text{crit}} \simeq 300 b^{-2} \left(\frac{1+z}{2} \right)^{1.8} \text{ deg}^{-2}. \quad (32)$$

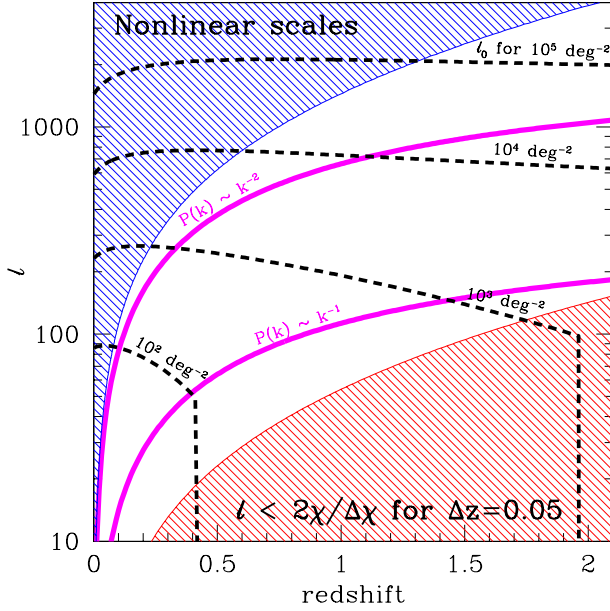


Figure 6. Shown are characteristic ℓ values for cross-correlation analyses as a function of z . The lower (red) shaded region delineates $\ell \leq 2\chi(z)/\Delta\chi$ for $\Delta z = 0.05$, approximately where the Limber approximation errors are tens of percent (Appendix B; Eq. B7). The upper (blue) shaded region is where deviations from linear perturbation theory are a factor of ≥ 2 . The other curves show characteristic scales at which $dN^{(p)}/dz$ estimates receive the bulk of their information. The dashed curves show the multipole where the Poisson term is equal to the clustering term, which we denote as ℓ_0 , for surveys with number densities of $b^2 dN/dz = 10^2, 10^3, 10^4$, and 10^5 deg^{-2} . The magenta curves are the scales where the density power spectrum has power-law index -2 and -1 , ℓ_{Pk-2} and ℓ_{Pk-1} , respectively. Correlations between two rare samples (where rare is defined as having $\ell_0 \lesssim \ell_{Pk-1}$) utilize modes with $\ell \sim \ell_{Pk-1}$ to constrain $dN^{(p)}/dz$. However, rare and abundant samples use modes with $\ell \sim \ell_{Pk-2}$, whereas if both samples are abundant the information comes from $\ell \sim \ell_0$ in certain cases.

Eq. 32 uses the Limber approximation, takes $f_{\text{sat}}^{(s)} = 0$, and approximates the redshift dependence as a power-law evaluated at $z = 1$. In addition, the lower horizontal line is the number density at which $w_i^{(s)} = [b_i^{(s)} N_i^{(s)}]^2 C_{ii}(\ell_{Pk-2})$, or

$$\left[\frac{dN}{dz} \right]_{-2}^{\text{crit}} \simeq 8000 b^{-2} \left(\frac{1+z}{2} \right)^{1.8} \text{ deg}^{-2}. \quad (33)$$

Both critical number densities are shown in Fig. 5 for our fiducial bias model. We return to the significance of these numbers in future sections.

We often will approximate the scale at which linear theory no longer holds as

$$k_{\text{NL}} \simeq 0.25 (1+z) \text{ Mpc}^{-1}, \quad (34)$$

which we find is close to the scale in which the Peacock & Dodds (1996) nonlinear density power spectrum overshoots linear theory by a factor of 2 for the redshifts of interest. We define $\ell_{\text{NL}} \equiv \chi k_{\text{NL}}$, which is plotted in Figs. 4 and 6 and throughout as the limit of validity of our assumptions. Fig. 6 shows that ℓ_0 falls in the range in which both linear theory and the Limber approximation more or less apply across all

k	n_{eff}	k	n_{eff}	k	n_{eff}
0.01	0.05	0.1	-1.7	1	-2.4
0.02	-0.7	0.2	-2.0	2	-2.5
0.05	-1.3	0.5	-2.3	5	-2.7

Table 2. The instantaneous power-law slope of the linear theory power spectrum as a function of wavenumber, k , in Mpc^{-1} ($n_{\text{eff}} \equiv d \log P / d \log k$). The values were computed using the Eisenstein & Hu (1998) matter transfer function without baryon acoustic features.

relevant redshifts and number densities. Linear theory also applies for ℓ_{Pk-1} and ℓ_{Pk-2} . We note that ℓ_{Pk-1} [ℓ_{Pk-2}] corresponds to a transverse physical scale of $k \simeq 0.03 \text{ Mpc}^{-1}$ [$k = 0.2 \text{ Mpc}^{-1}$] (Table 2).

3.2 The Schur-Limber limit

We now investigate the above Limber-approximation estimator in the limit $S(\ell) \rightarrow 1^+$ and show that a small tweak to this limit captures almost all of the information in the general case. We refer to the $S \rightarrow 1^+$ limit as the ‘Schur limit’ henceforth. In this limit the information originates from modes where $\sum_i r_i^2 \ll 1$, either because of incomplete overlap of the spectroscopic survey or because shot noise is important. In many interesting cases this limit at least marginally holds. Importantly, both **A** and **F** are diagonal in the Schur limit, viz

$$F_{ij}^S \approx \sum_{\ell, m} \frac{[A_{0i}]_{\ell}^2}{A_{00} A_{ii}} \delta_{ij}, \quad (35)$$

where the superscript S denotes the Schur limit. Furthermore, the estimator becomes

$$\hat{N}_i^{(p)} = [\hat{N}_i^{(p)}]_{\text{last}} + \frac{1}{F_{ii}^S} \sum_{\ell, m} \frac{[A_{0i}]_{\ell}}{A_{00} A_{ii}} \{ \hat{p} \hat{s}_i - A_{0i} \}, \quad (36)$$

such that the number density in each bin is now estimated independently and is proportional to the cross-power, $\hat{p} \hat{s}_i$, minus a constant. The Schur-Limit approximation yields the long-dashed blue curves for the errors on the $N_i^{(p)}$ shown in Fig. 2. These trace the contours in the full calculation (compare with the solid contours) at $dN/dz \lesssim 10^3 \text{ deg}^{-2}$, but begin to deviate if both samples have higher number densities, as is expected.

Two notes in passing: (1) The structure of F^S is reminiscent of the optimal weight in the Feldman et al. (1994) definition of the effective volume. While our expression is in harmonic space, the structure has the form $[\bar{n}P/(1+\bar{n}P)]^2$ just as in Feldman et al. (1994). This is not surprising as our estimator is asking a similar question to “What is the significance that the cross power can be detected?” (2) The Schur-Limber estimator is exact in the limits where Limber holds and $S = 1$, and does not require dropping certain derivative terms as was required to derive Eq. (31).

To see how the Schur-Limber estimator works, we take the case in which a single ℓ, m mode contributes to the estimate such that

$$\hat{N}_i^{(p)} = [\hat{N}_i^{(p)}]_{\text{last}} + \frac{\hat{p} \hat{s}_i - A_{0i}}{b_i^{(p)} N_i^{(s)} b_i^{(s)} C_{ii}}. \quad (37)$$

If the true $N_i^{(p)}$ differs from the fiducial model, $[N_i^{(p)}]_{\text{last}}$, by $\delta N_i^{(p)}$, we have the relations

$$\hat{p} \hat{s}_i = \left([N_i^{(p)}]_{\text{last}} + \delta N_i^{(p)} \right) N_i^{(s)} b_i^{(s)} b_i^{(p)} C_{ii}^{\text{data}} + w_i^{(ps)}, \quad (38)$$

where C_{ii}^{data} is the actual density power in this harmonic, and

$$A_{0i} = [N_i^{(p)}]_{\text{last}} \times N_i^{(s)} b_i^{(s)} b_i^{(p)} C_{ii} + w_i^{(ps)}. \quad (39)$$

Plugging these into Eq. (37) yields

$$\langle \hat{N}_i^{(p)} \rangle = [N_i^{(p)}]_{\text{last}} + \delta N_i^{(p)} = N_i^{(p)}, \quad (40)$$

noting that $\langle C_{ii}^{\text{data}}(\ell, m) \rangle = C_{ii}$. Thus, the iteration converges in a single step, and the estimate is unchanged with subsequent iterations. The former is no longer the case when multiple ℓ are used in the estimate, but we show that the estimator still converges in just a few iterations in Section 8.

The structure of the formula for the Fisher matrix in this Schur limit (Eq. 35) is also quite simple, and is most easily brought out by considering the case where the underlying power spectrum is a power-law, $C_{ii} = c_i \ell^n$ (we review some of the theory of power-law power spectra in Appendix E),

$$\mathbf{F}_{ij}^S = [N_i^{(p)}]^{-2} \sum_{\ell, m} \frac{c_i^{(p)} c_i^{(s)} \ell^{2n} \delta_{ij}^K}{(c^{(p)} \ell^n + w^{(p)}) (c_i^{(s)} \ell^n + w_i^{(s)})}, \quad (41)$$

where we have written $c_i^{(x)} = [N_i^{(x)} b_i^{(x)}]^2 c_i$, $c^{(p)} = \sum_i c_i^{(p)}$. The CDM case is similar, except that the spectrum has a power-law index which becomes increasingly negative towards smaller scales (see Table 2). Eq. (41) provides intuition into the shape of the contours in Fig. 2 as we shall now discuss.

3.3 Abundant galaxy limit

At ℓ where neither the photometric nor the spectroscopic survey is limited by shot noise, all ℓ contribute equally and the argument in the sum in Eq. (41) is roughly constant in ℓ . However, once shot noise becomes appreciable for either survey ($\ell > \ell_0$), the argument in the sum scales as ℓ^n . At scales where $n < -2$, which becomes increasingly satisfied at smaller scales with CDM spectra (see Table 2), this scaling cuts off the sum as shells of increasing ℓ contribute progressively less to \mathbf{F} . If $n > -2$, this is not true, and there is information until scales where both surveys are limited by shot noise (or n has steepened). This explanation is reflected by the contours in Fig. 2. For number densities where ℓ_0 occurs at scales at which $n < -2$ ($dN/dz > 8000 b^{-2} \text{ deg}^{-2}$), information is gained all the way until $\ell \sim \ell_0$. In this case, the contours are very boxy and Eq. (35) can be approximated as being clustering dominated at $\ell < \ell_0$ and being 0 at $\ell > \ell_0$:

$$\frac{\delta N_i^{(p)}}{N_i^{(p)}} \equiv \frac{\sqrt{[\mathbf{F}^S - 1]_{ii}}}{N_i^{(p)}} \sim (\langle \beta_i \rangle f_{\text{sky}} [\ell_0^2 - \ell_{\text{min}}^2])^{-1/2}, \quad (42)$$

where ℓ_{min} is the minimum wavenumber used, and $\langle \beta_i \rangle$ is the ℓ -averaged fraction of the angular power in the photometric

sample that comes from z -bin i :

$$\beta_i \equiv \frac{[N_i^{(p)} b_i^{(p)}]^2 C_{ii}(\ell, m)}{\sum_{j=1}^{N_{\text{bin}}} [N_j^{(p)} b_j^{(p)}]^2 C_{jj}(\ell, m)}. \quad (43)$$

For the simple case of slices of fixed number and distant observers (i.e., χ not changing appreciably across the sample), $\langle \beta \rangle \sim N_{\text{bin}}^{-1}$. The left panel in Fig. 7 shows how the sensitivity is increased with increasing $dN^{(p)}/dz$, fixing the photometric population (here a survey complete to $i = 23$) and the survey area. It shows that the prediction of Eq. (43) of a number density-independent error comes into full effect at $dN^{(s)}/dz > 10^5 \text{ deg}^{-2}$, which is on par with the maximum number densities that for medium-future experiments (see Fig. 1). Values of the Schur parameter greater than unity (Eq. 42 sets $S = 1$) result in some number density dependence even at high $dN^{(s)}/dz$.¹⁰ Also, evaluating Eqn. (42) for parameters that match the case given in the left panel of Fig. 7 – $\ell_0 = 2000$ (see Fig. 6), $\beta = 0.1$, and 100 deg^2 – yields $\delta N/N = 0.03$, which is comparable to the values for the largest $dN^{(s)}/dz$ in this plot.

We have used linear theory in our computations, but scales with $\ell > \ell_{\text{NL}}$ should not be used in our formalism. This nonlinear cutoff allows us to roughly estimate the smallest patch of sky for which cross-correlations will yield a useful constraint on $dN^{(p)}/dz$. Evaluating Eq. (42) with $\ell_0 \rightarrow \ell_{\text{NL}} \sim 10^3$ implies that a square degree is required for cross-correlations to provide an $\mathcal{O}(1)$ constraint on $dN^{(p)}/dz$ with our method. When accounting for $S > 1$, the constraint can improve by a factor of ~ 2 for physically realizable number densities (as can be gleaned by comparing the Schur estimator's error – the long-dashed blue curve – to the full estimator's error – the solid black curve – at high densities in Fig. 2).

3.4 Rare spectroscopic sample

Another relevant limit of the Schur-Limber estimator is when the spectroscopic sample is sparse enough that it is dominated by shot noise. In this limit, the Schur approximation ($S \approx 1$) is always justified, and our equations simplify further so that the Fisher matrix becomes

$$F_{ij} = N_i^{(s)} \sum_{\ell, m} \frac{[b_i^{(p)} b_i^{(s)} C_{ii}]^2 \delta_{ij}^K}{\sum_k (b_k^{(p)} N_k^{(p)})^2 C_{kk} + w_k^{(p)}} \propto N_i^{(s)} f_{\text{sky}}, \quad (44)$$

for $f_{\text{sat}} = 0$. Thus, in this limit the error on the $N_i^{(p)}$ scales as the total number of spectra – it does not depend on the density of spectroscopic sources. It turns out that in many relevant cases cross-correlations will be in this regime (as discussed in Section 4).

What $dN^{(s)}/dz$ are required to be in the rare limit? If $dN^{(s)}/dz < [\frac{dN}{dz}]_0^{\text{crit}}$, or roughly a hundred per square degree (Eq. 32), the sparse tracer limit certainly holds as

¹⁰ In fact, Eq. (42) should be regarded as an upper bound on the error since we set $S = 1$. When S is large (and here we take $w_i^{(s)} > w_i^{(p)}$ and $w_i^{(s)} > w_i^{(sp)}$, although similar conclusions apply regardless), $S \propto \sum_{i=1}^{N_{\text{bin}}} C_{ii}/w_i^{(s)}$. Including S in the summation in Eq. (41) makes the kernel peak at $\ell_{P_{k-2}}$ for high number densities rather than ℓ_0 . This results in the many-many case peaking at $\ell_{P_{k-2}}$ in Fig. 4.

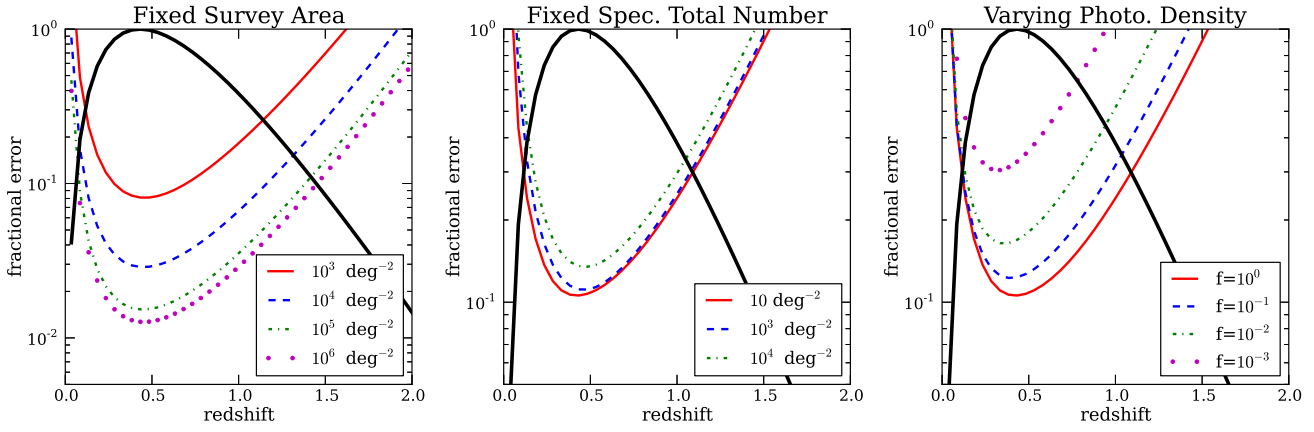


Figure 7. Illustration of how the fractional constraints on the $b_i^{(p)} N_i^{(p)}$ depend on area, total number, and densities of the samples. All panels take $\Delta z = 0.05$, a photometric sample down to a limiting magnitude of $i^{(p)} = 23$ (and 100 per cent complete except in the right panel), and a spectroscopic sample for which $dN^{(s)}/dz$ is a constant to $z = 2$. The $p(z|i)$ of the photometric sample is given by the thick solid curve. Left panel: The curves assume a 100 deg^2 survey and the specified $dN^{(s)}/dz$. At lower $dN^{(s)}/dz$ the sensitivity improves as the square root of $dN^{(s)}/dz$, as anticipated in the rare-spectra limit, but at high densities the sensitivity does not depend on depth, as anticipated by our abundant limit. Middle panel: The three curves show a spectroscopic sample with fixed total of 10^5 galaxies and the similarity of the sensitivity between these much different densities demonstrates our analytic result that in the rare tracer limit the fractional error scales as the total number of spectroscopic galaxies. Right panel: Varying the fraction, f , of photometric galaxies that are used with a spectroscopic sample with angular density 10 deg^{-2} , and 10^5 spectroscopic galaxies. In the limit in which both the photometric and spectroscopic samples are in the rare limit, the fractional sensitivity scales as $f^{-1/2}$. This addresses how well the distribution of an “interesting subsample” of objects could be determined.

the shot component always dominates. However, for even much larger number densities, the rare spectroscopic limit is a good approximation. The Fisher information at each ℓ for a rare spectroscopic sample (but abundant photometric sample) keeps increasing until $\ell_{P_{k-2}}$ (as $dF_{ii}^S/d\log \ell \propto \ell^{n+2}$ so that the contribution to F_{ii}^S decreases in bins of $\log \ell$ once $n < -2$). Thus, to be in the rare limit, it is less important that shot noise dominate at all ℓ and most important that shot noise dominates by $\ell_{P_{k-2}}$. Therefore, once $dN^{(s)}/dz < [dN/dz]_{-2}^{\text{crit}}$ (see Eq. 33) the rare limit applies, and the constraint on the $N_i^{(p)}$ only depends on the total number of galaxies.

The middle panel in Fig. 7 tests this argument that densities less than $[dN/dz]_{-2}^{\text{crit}}$ are in the rare limit. It plots the constraints on $b_i^{(p)} N_i^{(p)}$ for a photometric sample down to a limiting magnitude of $i = 23$, assuming $\Delta z = 0.05$. The three curves each take a spectroscopic sample comprised of 10^5 galaxies and differing $dN^{(s)}/dz$, where $dN^{(s)}/dz$ is taken to be constant up to $z = 2$ as specified in the figure key. Thus, the three curves represent surveys with the same number of spectroscopic galaxies. The sensitivity changes negligibly with number until 10^4 deg^{-2} .

The middle panel in Fig. 7, combined with our argument that $\delta N_i^{(p)} \propto [N_i^{(s)}]^{-1/2}$, where $N_i^{(s)}$ is the total number of spectroscopic galaxies per unit redshift, suggests that a minimum of $\sim 10^3$ spectroscopic galaxies are needed to have an order unity constraint on $b_i^{(p)} N_i^{(p)}$ (and somewhat fewer if the population is more localized in redshift than in our fiducial model). That $\sim 10^3$ spectroscopic galaxies are required is also apparent from evaluating Eq. (44) in the limits of a abundant photometric and rare spectroscopic survey,

which yields

$$\frac{\delta N_i^{(p)}}{N^{(p)}} \approx \frac{0.6}{b_i^{(s)} D_i} \left(\frac{N_i^{(s)}}{10^3} \frac{\langle \beta_i \rangle_C}{0.1} \right)^{-1/2} \left(\frac{1+z}{2} \right)^{-0.5}, \quad (45)$$

where we have assumed bins of fixed Δz , $\langle \beta_i \rangle_C$ is defined analogously to $\langle \beta_i \rangle$ but weighted by C_{ii} , and the redshift factor owes to how lengths map to angles and redshift intervals with z (which we evaluated at $z = 1$, but we find that this formula holds to 20 per cent for $0.1 < z < 3$).

3.5 Rare-rare limit

The final limit we consider is when the fluctuations in both samples are dominated by shot noise. In this limit, $dF_{ii}^S/d\log \ell \propto \ell^{2n+2}$ such that the contribution to F_{ii}^S decreases in bins of $\log \ell$ once $n < -1$. As with the abundant-rare limit previously considered, we can also evaluate Eq. (35) in the rare-rare limit, which yields

$$\frac{\delta N_i^{(p)}}{N^{(p)}} \approx \frac{1.7}{b_i^{(s)} b_i^{(p)} D_i^2} \left(\frac{N_i^{(s)}}{10^3} \frac{dN_i^{(p)}/dz}{10^2 \text{ deg}^{-2}} \frac{f_i}{0.1} \right)^{-1/2} \left(\frac{1+z}{2} \right)^{0.4}, \quad (46)$$

where f_i is the fraction of the photometric galaxies in redshift bin i (and equals the distant observer β_i in the case of redshift independent clustering). This expression shows that $N_i^{(s)} \times dN_i^{(p)}/dz \gtrsim 10^6 \text{ deg}^{-2}$ is required for cross-correlations to be fruitful. The right panel in Fig. 7 shows the constraints on the $N_i^{(p)}$, again with the specifications $i^{(p)} = 23$ and 10^5 total spectroscopic galaxies, but taking $dN^{(s)}/dz = 10 \text{ deg}^{-2}$ for all the curves and assuming that only a fraction, f , of photometric galaxies are used in the cross correlations. When both the photometric and spectroscopic galaxies are in the rare limit, Eq. (46) shows that the

sensitivity scales as $f^{-1/2}$. We note that the peak of dN/dz for a survey complete to $i = 23$ equals $5 \times 10^4 \text{ deg}^{-2}$, so the $f \lesssim 0.01$ curves should be in this limit, and we indeed find this scaling in this regime. This panel illustrates that cross-correlations can be used to constrain the redshift distribution of peculiar objects, comprising a part in 10^3 of the photometric sample in the case shown, and not just the full sample.

The derivations that led to Eq. (46) implicitly assumed that the bias of the spectroscopic sample is known from auto-correlation function measurements. However, in the limit of a rare spectroscopic sample, the auto correlations can be much noisier than the cross correlations, calling into question this assumption. We show in Appendix A2 that in this case the fractional variance on the $N_i^{(p)}$ is simply the fractional variance quoted in this section added to the fractional variance in the bias measurement.

Because the two limits given by Eqs. (45) and (46) yield similar $\delta N(z)/N(z)$ at the transition between the two regimes (at $dN^{(p)}/dz \sim 0.1 [dN^{(p)}/dz]_{-2}^{\text{crit}}$), the sensitivity of an arbitrary photometric survey can be obtained by interpolating between them.

3.6 Generalizing the Schur Limit

We showed that in the Schur-Limber limit the Fisher matrix is diagonal. However, empirically we find that the off-diagonal terms in Eq. (30) are generally unimportant for determining the uncertainty in the $N_i^{(p)}$: The dashed green contours in Fig. 2 show the impact of dropping the off-diagonal term in Eq. (30), but keeping the S factors so that $\mathbf{F}(\ell) = S \mathbf{F}^S(\ell)$ and similarly S appears in the summation in the estimator. This “generalized” estimator is unbiased. Empirically, this approximation (the short-dashed green curves) differs from the full Fisher Matrix (the solid black contours) by a factor of $\sim 1 - N_{\text{bin}}^{-1} \approx 0.9$.

There are several idealized cases where one can show that dropping the off-diagonal elements of \mathbf{F} is a good approximation to $\sim 1 - N_{\text{bin}}^{-1}$ (such as the case of a single ℓ), but only our numerical results can be used to justify the result in general. The approximation of ignoring off diagonals when computing the estimator variance from \mathbf{F} is equivalent to not marginalizing over parameters other than $N_i^{(p)}$. That \mathbf{F}^{-1} is approximately diagonal thus means that one does not have to simultaneously estimate each of the $[\hat{N}_i^{(p)}]$ and rather can estimate each parameter independently for $[\hat{N}_i^{(p)}]_{\text{last}}$ near the peak likelihood.

4 APPLICATIONS

The previous section built intuition for the behavior of, and relevant scales for, the estimator. To bring out the appropriate limits we considered simple dN/dz distributions, such as constants. This section considers more physically motivated parameterizations for the galactic populations. Fig. 8 is analogous to Fig. 4 but quantifies the scales that contribute to the constraint on the $N_i^{(p)}$ for *realistic* source models, plotting $d[1/\mathbf{F}_{ii}^{-1}]/d \log \ell$. In particular, Fig. 8 considers the models:

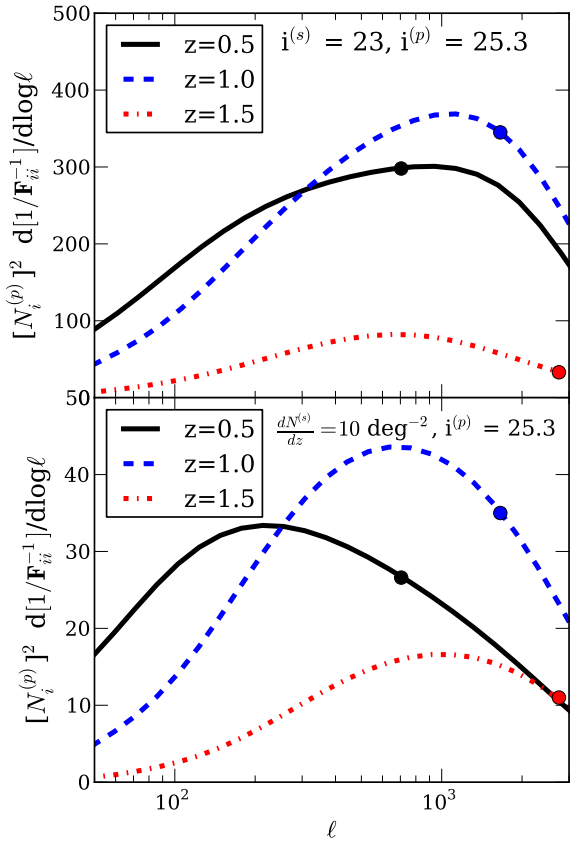


Figure 8. Similar to Fig. 4, but for more physical cases. Plotted is the information as a function of ℓ , $d[1/\mathbf{F}_{ii}^{-1}]/d \log \ell$. The variance in $N_i^{(p)}$ is the inverse of the area under these curves. The filled circles show $\ell_{\text{NL}} \equiv \chi^2 k_{\text{NL}}$ (c.f., Eq. 34). The top (bottom) panel considers a 40 deg^2 (10^4 deg^2) survey and takes bins of $\Delta z = 0.05$ spanning $0 < z < 2.5$.

top panel: $i^{(s)} = 23$ over 40 deg^2 , and $i^{(p)} = 25.3$, characteristic of the LSST gold sample,

bottom panel: $dN^{(s)}/dz = 10 \text{ deg}^{-2}$ over 10^4 deg^2 and $0 < z < 2.5$, characteristic of SDSS quasars, and again $i^{(p)} = 25.3$.

In the model in the bottom panel, the kernel peaks near the scale ℓ_{Pk-2} , which corresponds to $\ell = 400, 700$ and 900 at $z = 0.5, 1$, and 1.5 . This is as expected when at least one sample is abundant. In the model in the top panel, the information has a broad peak that falls between ℓ_{Pk-2} and ℓ_0 , where $\ell_0 = 800, 2000$, and 3000 for the three redshifts considered. This is consistent with our arguments for the case of two abundant samples. In both of the models considered in Fig. 8, the majority of the information arises from linear scales (scales which fall leftward of the filled dot, representing ℓ_{NL} , on each curve). We find similar conclusions apply for a range of models.

Fig. 9 investigates the tradeoffs of depth versus area for attempts to constrain the $N_i^{(p)}$ in 50 redshift bins with $\Delta z = 0.05$ and spanning $0 < z < 2.5$. The top panel is for a photometric sample with the specifications of the LSST gold sample (which has $dN^{(p)}/dz > 10^4 \text{ deg}^{-2}$ over the entire redshift range) and for three spectroscopic samples that could be obtained with the same total time on a telescope. (More

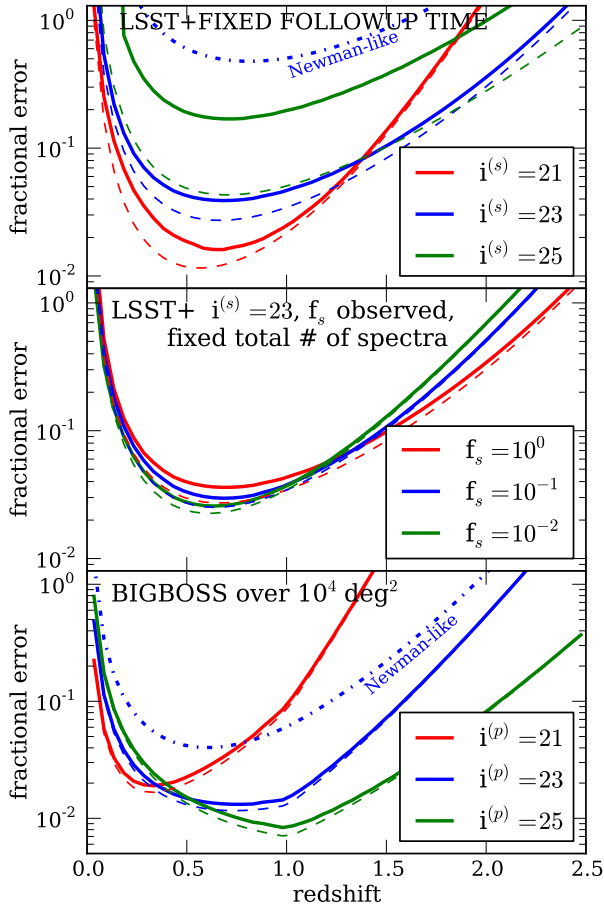


Figure 9. Shown are estimates for the sensitivity to reconstruct redshifts of a photometric sample in redshift bins of $\Delta z = 0.05$ and spanning $0 < z < 2.5$. The top panel is for a photometric sample with the specifications of the LSST gold sample ($i^{(p)} = 25.3$; see text) and for different spectroscopic samples that could be obtained for the same total telescope time: The spectroscopic followup covers 1 deg^2 to $i^{(s)} = 25$, 40 deg^2 to $i^{(s)} = 23$, or $1,600 \text{ deg}^2$ to $i^{(s)} = 21$. The middle panel is similar to the top panel but assumes f_s of galaxies to $i^{(s)} = 23$ are observed over a region of $40 f_s^{-1} \text{ deg}^2$. The bottom panel is for a spectroscopic sample with the specifications of BigBOSS and the specified limiting photometric magnitudes. This panel assumes that the surveys' overlap is 10^4 deg^2 , but the quoted error scales as the square root of the survey area. In both panels, the dashed curves use all ℓ values, whereas the solid exclude information from $\ell > \ell_{\text{NL}}$. The dot-dashed curves (shown only for the $i = 23$ case) in the top and bottom panels are the variance of the Newman-analog estimator without any cutoff at nonlinear scales.

correctly, the limiting flux squared divided by the survey area is held constant.) We assume that the spectroscopic followup covers 40 deg^2 at $i^{(s)} = 23$. Hence, it covers $1,600 \text{ deg}^2$ at $i^{(s)} = 21$ and 1.0 deg^2 at $i^{(s)} = 25$. This panel illustrates that deeper is not necessarily better (compare only the solid curves for the time being). This conclusion arises because the spectroscopic galaxies are more or less in the abundant limit (particularly near their peak in $dN^{(s)}/dz$) where the fractional error does not depend on depth and instead scales as $f_{\text{sky}}^{1/2}$. However, the scaling $f_{\text{sky}}^{1/2}$ – a factor of 6 between the three cases considered in the top panel – over predicts

what is seen in this panel. This arises because these samples are only marginally in the dN/dz regime where we find this scaling holds (Fig. 7) and also because $S > 1$ breaks this scaling, which was derived in the $S = 1$ limit. The $i^{(s)} = 21$ sample is in the rare sample limit at the highest redshifts shown, and hence its errors blow up there. By contrast, while the $i^{(s)} = 25$ sample is the least sensitive to $dN^{(p)}/dz$ at intermediate redshifts (owing to its small f_{sky}), it is the most able to determine the distribution at the highest redshifts.

The middle panel in Fig. 9 is similar to the top panel but assumes a random fraction, f_s , of all galaxies with $i^{(s)} = 23$ are observed over a region of $40 f_s^{-1} \text{ deg}^2$ such that the total number of galaxies is fixed. This panel reinforces our result that the constraint on the $N_i^{(p)}$ depends primarily on the total number of spectroscopic galaxies and not their angular density, even though the case with $f_s = 1$ is in our abundant limit in which we no longer expect this scaling to hold. We still find this result *approximately* holds.

The bottom panel in Fig. 9 shows the case of a spectroscopic sample with the specifications of BigBOSS (whose dN/dz is shown in Fig. 1) and the specified limiting photometric magnitudes.¹¹ This panel assumes that the surveys' overlap is 10^4 deg^2 , but the error scales as the square root of the overlapping area. Despite the lower number densities of galaxies in this case compared to in the top panel, BigBOSS has a total number of galaxies that exceeds the other cases by more than an order of magnitude and, thus, is the most sensitive of all the cross-correlation examples considered in Fig. 9. These sensitivity predictions are in qualitative agreement with our previous estimate for the rare case: evaluating Eq. (45) for $\mathcal{N}^{(s)} = 10^7$ galaxies and $\beta = 0.1$ yields 0.01, in qualitative agreement with the sensitivity minimum in Fig. 9. We note that to reach the 10^{-2} sensitivity quoted here, BigBOSS would likely need to correct for magnification bias (which is discussed in Section 6).

Omitting nonlinear scales or introducing a redshift cutoff in the spectroscopic coverage has little impact on our results. The dashed curves in Fig. 9 include information from $\ell > \ell_{\text{NL}}$, whereas the solid curves do not. Excluding nonlinear modes in the analysis has only a modest impact on the estimator, except in the $i^{(s)} = 25$ case in the top panel, where the constraint is reduced by a factor of 3. This case is most impacted because (1) its ℓ_0 falls at the most nonlinear scales of the cases plotted and (2) the small 1 deg field assumed in this case has already limited the scales that can contribute. Similar losses for each of the plotted case also occur for a factor of 2 smaller ℓ_{NL} . In addition, we have assumed the spectroscopic sample spans the entire redshift range of the photometric sample. A cutoff in the coverage of a spectroscopic sample, as could occur if an emission line falls out of the spectroscopic band of a survey, has little impact on our results below that cutoff. It has no impact to the extent that $S = 1$, which more or less holds for all cases shown in Fig. 9, with the largest differences occurring for the deepest case considered in the top panel: when the additional condition $dN^{(s)}/dz = 0$ was imposed for $z > 1.5$, which

¹¹ BigBOSS aims for a combined dN/dz that we crudely parametrize as $30 \times 10^{2.1} z \text{ deg}^2$ for $z < 1.0$ and $4000 \times 10^{-1.1} (z-1) \text{ deg}^2$, to approximate what is quoted at <http://bigboss.lbl.gov>.

forces S to be small, we found no change to the $i^{(s)} = 21$ case in the top panel, but a factor of 2.5 shift upward for $i^{(s)} = 25$.

The photometric sample can often be divided into magnitude bins or into photometric redshift bins. For magnitude cuts, extra sensitivity is often gained by dividing the primary photometric sample because galaxies in different magnitude bins are more likely to also be at different redshifts (as suggested by the top panel in Fig. 9). In particular, in the rare spectroscopic galaxy limit but where the photometric galaxies are more abundant than $[dN/dz]_{-2}^{\text{crit}}$, the signal scales inversely with the redshift extent of the photometric sample and does not depend on the $dN^{(p)}/dz$ (Eq. 45). Thus, the sensitivity is not improved by going deeper. The redshift distribution of galaxies given by our parameterization for $P(z|i)$ (Eq. 3) has mean $3z_0$ and variance $3z_0^2$. Because the variance of $P(z|i)$ increases with depth, deeper surveys will be somewhat less sensitive at the peak of $P(z|i)$ unless the sample is partitioned.¹² A partitioned sample can be easily accommodated in our quadratic estimator formalism. In Section 7, we discuss the gains from dividing by photometric redshift.

5 CONFIGURATION SPACE

The previous derivations were done in spherical harmonic space as this is the simplest basis for calculating the minimum variance estimator. However, when dealing with actual data it can be more difficult to work with spherical harmonics as the survey window function enters nontrivially in convolution. Hence many galaxy clustering analyses are done in configuration space. In this section we show that the minimum variance estimator can be easily applied in this dual space (Section 5.1), we compare with previous configuration space dN/dz estimators (Section 5.2), and finally discuss the impact of finite sky coverage (Section 5.3)

5.1 Configuration space estimator

The harmonic space quadratic estimator can be written in the form

$$\sum_{\ell, m} v_i(\ell) \hat{p}(\ell, m) \hat{s}_i(\ell, m), \quad (47)$$

for some $v_i(\ell)$, plus analogous terms proportional to the auto correlations. Writing $\hat{p} \hat{s}_i(\ell, m) = \int d\hat{n} \hat{p} \hat{s}_i(\hat{n}) Y_\ell^m(\hat{n})$, Eq. (47) becomes

$$\int d\hat{n} d\hat{n}' \hat{p}(\hat{n}') v_i(\hat{n} \cdot \hat{n}') \hat{s}_i(\hat{n}), \quad (48)$$

where we have used the addition theorem for spherical harmonics (Abramowitz & Stegun 1972), P_ℓ is the Legendre polynomial of order ℓ , and

$$v_i(x) = \sum_{\ell} \frac{2\ell+1}{4\pi} v_i(\ell) P_\ell(x). \quad (49)$$

¹² This statement holds as long as $dN^{(p)}/dz > [dN/dz]_{-2}^{\text{crit}}$. This inequality is satisfied near the peak of $P(z|i)$ down to the lowest magnitudes for which Eq. (3) is calibrated, $i = 20.5$ (see Fig. 1).

If we define $\hat{\omega}_{ps_i}(x) \equiv \langle \hat{p} \hat{s}_i \rangle_x$, as the correlation function estimate where $x = \hat{n} \cdot \hat{n}'$ and $\langle \dots \rangle_x$ represents an average over all separation angles x in the survey, Eq. (48) can be re-expressed as

$$8\pi^2 \int dx v_i(x) \hat{\omega}_{ps_i}(x). \quad (50)$$

Thus, the configuration space estimator in the Schur-Limber limit is

$$\begin{aligned} [\hat{N}_i^{(p)}] &= [\hat{N}_i^{(p)}]_{\text{last}} + \frac{8\pi^2}{F_{ii}} \sum_{\alpha} \Delta x_{\alpha} v_i(x_{\alpha}) \\ &\times \left\{ \hat{\omega}_{ps_i}(x_{\alpha}) - \omega_{ps_i}(x_{\alpha}) \right\}, \end{aligned} \quad (51)$$

where α runs over the bins in (cosine of the) angle. A similar configuration space estimator can be written for the full minimum variance quadratic estimator (Eq. 16).

For $\theta \ll 1$ radian (the scales that we will show are of primary interest), the result can be further simplified by making the flat sky approximation. Then, the Parseval identity, $\int d^2\ell v_i^*(\ell) \hat{p} \hat{s}(\ell) / (2\pi)^2 = \int d^2\theta v(\theta) \hat{p} \hat{s}(\theta)$, can be directly applied to Eq. (47) to yield Eq. (51) with $\Delta x_{\alpha} \rightarrow \theta_{\alpha} \Delta\theta_{\alpha}$ and

$$v_i(\theta) = \int_0^{\infty} \frac{\ell d\ell}{2\pi} v_i(\ell) J_0(\ell\theta). \quad (52)$$

The same expression can be derived from Eq. (49) by writing the small-angle limit of P_ℓ in terms of J_0 (Abramowitz & Stegun 1972).

We note that in the Schur-Limber limit

$$v_i(\ell) = \frac{b_i^{(p)} b_i^{(s)} N_i^{(s)} C_{ii}}{\left[\sum_i \left(b_i^{(p)} N_i^{(p)} \right)^2 C_{ii} + w_i^{(p)} \right] \left[\left(b_i^{(s)} N_i^{(s)} \right)^2 C_{ii} + w_i^{(s)} \right]}. \quad (53)$$

The thick curves in the top panel in Fig. 10 show the flat sky weighting kernel for the same example surveys as in Fig. 4, down weighting nonlinear modes by multiplying $v_i(\ell)$ by the factor $\exp[-\ell^2/\ell_{\text{NL}}^2]$. These calculations show that if any sample is in the abundant limit, the window peaks at $\theta \sim 0.1$ deg separations, whereas if both surveys are in the rare limit the peak occurs at $\theta \sim 1$ deg. Both cases have non-negligible weight at super-degree scales.

The bottom panel in Fig. 10 shows $\theta v_i(\theta) \times \omega_{ps_i}$, which better represents the θ that contribute to the final estimate. Since measured correlations are weaker on large scales than small, the $\theta > 1$ deg behavior of $v_i(\theta)$ is down-weighted and really only sub-degree scales contribute significantly.

In practice, whether weights are applied during or after the computation of the correlation function depends on the survey to which cross-correlations are applied. In the case where the survey's contiguous area is much larger than the kernel of $v_i(x)$ ($\gg 0.1-1$ deg), the exact details of the survey window are irrelevant. The $\omega_{ps_i}(\theta)$ can be estimated with standard techniques (e.g. Landy & Szalay 1993; Hamilton 1993; Bernstein 1994) and then multiplied by the approximate v_i . This is the regime most large-scale photometric and spectroscopic surveys, such as SDSS, WiggleZ, BOSS, GAMA, DES, and LSST. The second regime, where the survey area is comparable to or smaller than the weighting kernel (e.g. with DEEP or HST fields) is more complex. Section 5.3 discusses this case.

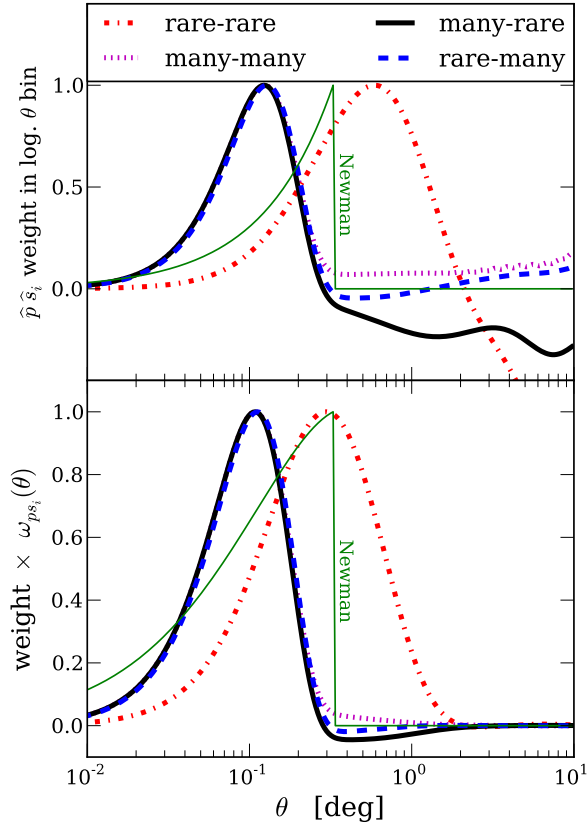


Figure 10. The top panel shows the configuration-space weights of the optimal estimator, $\theta \times v_i(\theta)$, in the Limber and flat sky approximations for the illustrative cases considered in Fig. 4, again for the $i = 6$ redshift bin. The bottom panel shows this times the angular correlation function, ω_{ps_i} , which shows explicitly which angular scales the information derives. The thin solid green curve in each panel is the weighting scheme used in our analog of the Newman (2008) estimator, with $r_{\max} = 10 h^{-1}\text{Mpc}$. All of the curves, aside from the Newman-analog ones, have down weighted nonlinear modes by the factor $\exp[-\ell^2/\ell_{\text{NL}}^2]$.

5.2 Comparison to earlier work

Using cross-correlations to estimate redshift distributions has been championed recently by Newman (2008) and Matthews & Newman (2010). The configuration space expression for the optimal quadratic estimator (c.f., Eq. 51) allows us to compare explicitly with the Newman (2008) method. Though the Newman (2008) method is neither optimal nor unbiased, it has some similarities to our estimator as we shall see.

The estimator in Newman (2008) and Matthews & Newman (2010) is fairly complicated, as it involves nonlinear, power-law fits to correlation functions over a specified range of scales and with specified, diagonal (i.e. ignoring bin-to-bin correlations in θ and z) weights. The estimator is thus a non-linear functional of the measured 2-point functions. However since the power-law fit is used mainly to divide out trends and fit for an amplitude, we can write an *analogous* estimator to Newman (2008) that contains essentially the same

information. Our analog-estimator becomes very similar to that of Newman (2008) for power-law models.¹³

Our analog of the Newman (2008) estimator is¹⁴

$$\hat{N}_i^{(p)} = \eta_i^{-1} \sum v_i^{\text{New}} \left(\hat{p} \hat{s}_i - w_i^{(ps)} \right), \quad (54)$$

where

$$\eta_i = \left(\sum v_i^{\text{New}} b_i^{(p)} b_i^{(s)} N_i^{(s)} C_{ii} \right). \quad (55)$$

This estimator returns $N_i^{(p)}$ if the Limber approximation holds and the underlying power spectra and biases are correctly guessed. When the sum in Eq. (54) is over configuration space pixels (as in Newman 2008), the weighting is

$$v_i^{\text{New}}(r) = \begin{cases} 1 & r_{\min} < r < r_{\max} \\ 0 & \text{otherwise} \end{cases} \quad (56)$$

where Newman (2008) chooses $r_{\min} = 0$ and $r_{\max} = 10 h^{-1}\text{Mpc}$. Fig. 10 compares the weights of our optimal estimator to that of our Newman-analog estimator. The thin green solid curve in the top panel is $\theta v_i^{\text{New}}(\theta)$ and in the bottom panel this curve is $\theta v_i^{\text{New}}(\theta) \times \omega_{ps_i}$. The thick curves are this same quantity for the optimal estimator for the same four extreme cases as considered earlier. The Newman-analog estimator uses similar scales to those selected by the optimal estimator, especially in the rare-rare case.

While the weights for the optimal quadratic and Newman-analog estimators are superficially similar, it becomes apparent that the estimators behave differently when examining the weights in more detail. The optimal estimator in the shot noise-limited regime has configuration-space weights given by the density correlation function. However, the Newman-analog weights are simply a constant. The structure of the Newman-analog estimator is also much different in the signal-dominated regime. The optimal estimator has weight $v_i(\theta) \propto \int \ell d\ell S C_{ii}^{-1} J_0(\ell\theta)$, assuming the Limber and diagonal estimator approximations, in contrast to the constant configuration space weights assumed in the Newman analog.

The variance of these estimators also differ. The covariance of the minimum variance estimator is \mathbf{F}^{-1} , whereas the covariance of the Newman-analog estimator (in the Limber approximation) is

$$\begin{aligned} \text{cov}[\hat{N}_i^{(p)}, \hat{N}_j^{(p)}] &= \eta_i^{-1} \eta_j^{-1} \sum_{\ell, m} v_i^{\text{New}}(\ell) v_j^{\text{New}}(\ell) \\ &\times \left[A_{0i}(\ell) A_{0j}(\ell) + A_{00}(\ell) A_{ii}(\ell) \delta_{ij}^K \right], \end{aligned} \quad (57)$$

where the Fourier space (flat sky) Newman weights are the

¹³ We must further assume that the power-law slope of the spectroscopic sample equals that for the photometric sample. On large scales this is guaranteed, as both trace the matter power spectrum. However on small scales it depends on the manner in which objects populate haloes. Newman (2008) and Matthews & Newman (2010) assume that the cross-correlation function is the geometric mean of the auto-correlation functions.

¹⁴ While Newman (2008) does not explicitly subtract a shot-noise term, we have subtracted $w_i^{(ps)}$ so that the estimator is well-defined in both configuration and harmonic space.

Hankle transform of eqn. (56):

$$v_i^{\text{New}}(\ell) = \frac{\chi_i}{\ell} \left(\frac{J_1(\ell r_{\text{max}}/\chi_i)}{r_{\text{max}}} - \frac{J_1(\ell r_{\text{min}}/\chi_i)}{r_{\text{min}}} \right). \quad (58)$$

The rapid oscillations at higher ℓ damp the contribution of these modes. The dot-dashed curves in Fig. 9 (shown only for the $i = 23$ case) in the top and bottom panels are the variance of the Newman-analog estimator without any nonlinear cutoff in ℓ . The Newman-analog estimator performs substantially worse than the optimal estimator: a factor of 3–10, with the factor of 10 applying to the abundant galaxy case (which is most similar to the cases investigated in Newman 2008 and Matthews & Newman 2010).

5.3 Finite sky coverage

Until now many of our expressions have implicitly assumed that the surveys cover the full sky, which is unlikely to be the case in practice. For surveys whose narrowest dimension is much larger than the scales where our estimator peaks, the correction for finite sky coverage is benign: we simply have a factor of f_{sky} to correct the number of modes in our Fisher matrix (e.g. Scott et al. 1994; Jungman et al. 1996; Tegmark 1996; Knox 1997), as we have assumed in our prior example calculations. The effects of finite sky coverage have been studied extensively in the CMB (e.g. Hivon et al. 2002; Hansen et al. 2002; Efstathiou 2004) and large-scale structure literature (e.g. Feldman et al. 1994; Peacock & Nicholson 1991; Park et al. 1994; Tegmark et al. 1998).

If the area of the sky covered by the calibrating, spectroscopic survey is small (\lesssim a few deg. on a side) then the effects of the window function (the function that describes a survey's sky coverage) become important as our estimator uses separations out to ~ 1 deg (especially in the case in which both samples are sparse). In this case we can safely make the flat sky approximation in which case our harmonic-space description is a Fourier-space description. In this case, the minimum variance quadratic cross-correlation estimator for $N_i^{(p)}$ takes the form

$$\int \frac{d^2 k_1 d^2 k_2}{(2\pi)^4} \hat{p}(\mathbf{k}_1) Q(\mathbf{k}_1, \mathbf{k}_2) \hat{s}_i(\mathbf{k}_2) \quad (59)$$

where Q is a kernel which is no longer diagonal in \mathbf{k} -space.

The case of a general survey window function can be complex, but, if the width and height of the window are comparable, the effects of windowing are easily understood. Due to the convolution with the window function, k -modes which are separated by less than $2\pi/\Theta$ (where Θ is the angular extent of the window function) are almost completely correlated and, thus, contain largely redundant information. Whereas, for modes separated by much more than $2\pi/\Theta$, the effects of the window function can be largely ignored.

Thus the effects of finite sky coverage can be taken into account by replacing our sums over ℓ with sums over L values which are integer multiples of $2\pi/\Theta$ and defining the C_L as bin-averages of the C_ℓ . A simpler approximation, valid if the theoretical spectra are smooth, is to simply integrate from $2\pi/\Theta$ to infinity rather than zero to infinity in Eq. (52). If in computing the correlation function or power spectrum we estimate the mean density from the survey itself, then the power is suppressed on large scales (often known as the integral constraint; Peebles 1980). An approximation to this

suppression is to multiply C_ℓ by $|1 - W(\ell)|^2$ where $W(\ell)$ is the window function normalized so that $W \rightarrow 1$ as $\ell \rightarrow 0$.

6 BIAS OF APPROXIMATE ESTIMATORS

The minimum variance quadratic estimator under the approximation that off-diagonal terms in the Fisher matrix are zero is unbiased as long as the diagonal entries are appropriately calculated. In addition, dropping derivative terms in the quadratic estimator is unbiased since each derivative explores separate dependences. However, there are a few approximations that could incur bias: the Limber approximation, ignoring RSDs, including nonlinear scales, cosmic magnification, and assuming the incorrect cosmology. We do not consider the latter because it should be reduced to the per cent-level with the coming generation of cosmological probes, but we consider the others.¹⁵ If the bias is small, it can be easily computed by substituting the full $\langle (\hat{p} \hat{\mathbf{s}})^\dagger \times (\hat{p} \hat{\mathbf{s}}) \rangle$ that includes the ignored terms into the approximate estimator and evaluating both near the input $N_i^{(p)}$. Using this formalism, we address these biases here.

Limber approximation and RSDs:

In the Limber approximation, which has been assumed by most previous investigations of dN/dz estimation from cross-correlations, the diagonals are accurately estimated in the limit $\ell \Delta\chi \gg \chi$ (although, in practice this condition has to be just weakly satisfied). Fig. 6 suggests that most scales that contribute to our estimate are safely in this Limber regime for $\Delta z \sim 0.1$. This will be less true for smaller Δz . On angular scales favored by our estimator, at which the matter power spectrum is decreasing with increasing k , the Limber approximation results in an over-prediction of the C_{ii} . Hence, the our Schur-Limber estimator will result in an under-prediction. However, setting to zero the $\langle p_i s_j \rangle$ for $i \neq j$ in the Limber approximation has the opposite effect. We find that the former effect is larger such that Limber results in an under-prediction, with a fractional error of $-(2-3) \times 10^{-3}$ for $\Delta z = 0.01$ and $0 < z < 1$ for cases where most of the information derives from ℓ_{Pk-2} (i.e., where one of the populations is abundant) and $-(0.3-1) \times 10^{-2}$ for cases where most of the information derives from ℓ_{Pk-1} .¹⁶ For $\Delta z = 0.1$, the biases are of course significantly smaller than for $\Delta z = 0.01$. Thus, the Limber approximation will likely result in a bias that is smaller than the estimator's variance even for applications with very large source populations. A corollary of Limber being a good approximation is that extra sensitivity to the $N_i^{(p)}$ does not arise by first estimating them in redshift bins with smaller redshift intervals than the desired Δz for $\Delta z \gtrsim 0.1$. (Fig. 3 suggests that there is some extra information for $\Delta z = 0.01$ as the Limber estimate errors differ.)

The fact that the Limber approximation is as successful as it is suggests that redshift space distortions (RSDs) will

¹⁵ If dN/dz is being estimated as part of a program aimed at constraining the cosmology, e.g. with gravitational lensing, the cosmology and dN/dz will have to be simultaneously varied.

¹⁶ We speculate that the surprising smallness of the biases in Limber results because of a near cancellation of the two competing effects.

also induce a small bias (as RSDs are negligible on scales at which the Limber approximation holds; Appendix B). However, for reasons discussed in Appendix B, including RSDs is difficult in our current formalism as it requires a basis switch from our choice of top hat redshift bins, which spuriously magnify the impact of RSDs. Thus, we do not quantify the magnitude of their small bias on the estimator.

Nonlinear scales and the one halo term:

Using scales that are nonlinear can bias the estimator. The Schur-Limber estimator for $N_i^{(p)}$ is biased by nonlinear effects that occur at the redshift of the estimate, z_i , and (fortunately) not by nonlinearities at other redshifts. This is not the case for the minimum variance quadratic estimator (a fact that we have ignored). In our estimates in Section 4 and Fig. 9, we masked nonlinear wavenumbers at z_i that met the criterion $k > k_{\text{NL}}(z_i)$ (defined in Eq. 34), and found that this operation does not have a large impact on the sensitivity, except for the densest samples that were considered. This result owes to the broad range in ℓ that contributes the information, which generally peaks at $\ell < \ell_{\text{NL}}$ (Fig. 4). We find that if we reduce k_{NL} by an additional factor of 2, which corresponds to a wavenumber where the nonlinear density power spectrum deviates from linear theory by just 10 per cent, the constraints are additionally degraded by a similarly small factor.

As long as they are modeled properly, nonlinearities that trace the density field do not necessarily bias a measurement of $N_i^{(p)}$ as the galaxies still trace the same large-scale density fluctuations. A bias will arise if intra-halo correlations contribute at scales where they are not in the white noise regime (as we have assumed). Fortunately, deviations from the large-scale limit generally occur at wavenumbers that are larger than k_{NL} , especially if clusters and large, low-redshift groups are excluded from the cross-correlation analysis (see plots in Cooray & Sheth 2002).

Magnification bias:

Magnification bias is the most significant of the biases we considered. Cosmic magnification results in additional off-diagonal terms in \mathbf{C} that were zero in the Limber approximation. These terms are suppressed relative to the $j - j$, diagonal Limber term (Eq. 21) by the factor

$$R_{ij}^{(x)} \equiv -\frac{\alpha_i^{(x)} + 1}{b_j^{(x)}} \left[\frac{(1 + z_j) \chi_j \Delta \chi_j}{2 \times 10^7 \text{ Mpc}^2} \right] \left(1 - \frac{\chi_j}{\chi_i} \right) \quad (60)$$

for $i > j$, where $\alpha_i^{(x)}$ is the power-law index of the cumulative source number counts in bin i above a certain flux threshold (see Appendix C). Eq. (60) ignores magnification-magnification correlations, which are smaller except perhaps for surveys at $z \gg 1$.

For our simple Schur-Limber estimator, it is easy to compute the $N_i^{(p)}$ estimator bias, being

$$\text{frac. bias from mag.} = \sum_{k, k > i} \frac{N_k^{(p)}}{N_i^{(p)}} R_{ki}^{(p)} + \sum_{k, k < i} \frac{N_k^{(p)} C_{kk}}{N_i^{(p)} C_{ii}} R_{ik}^{(s)}, \quad (61)$$

where C_{ii} is defined in Eq. (21). Thus, this estimator results in an overestimate when $-\alpha^{(x)} - 1 > 0$. Evaluating this for our toy case of constant dN/dz from $0 < z < 1$, one finds a

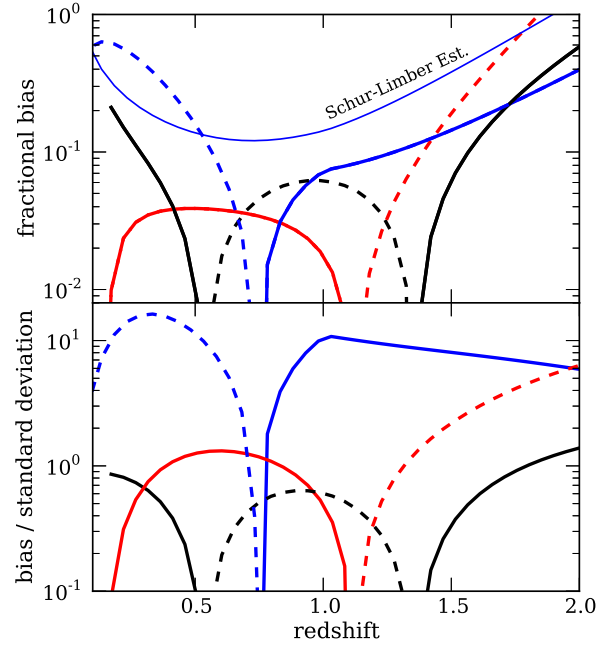


Figure 11. The estimator bias arising from magnification for estimators that ignore this effect. The curves assume that the photometric sample consists of all galaxies with $i^{(p)} < 25.3$ and $0 < z < 2.5$ (the bias will be smaller in lower redshift samples) and different spectroscopic samples. The thick blue curves are the full quadratic estimator for BigBOSS and an overlap area of 10^4 deg^2 , the black curves are $dN^{(s)}/dz = 10 \text{ deg}^{-2}$ covering $0 < z < 2.5$ and over 10^4 deg^2 , and the red curves are an example survey with $i^{(s)} = 23$ and 40 deg^2 . Solid (dashed) curves indicate that the bias results in an overestimate (underestimate). The top panel is the bias relative to $N_i^{(p)}$, and the bottom panel is this relative to the fractional error. All curves simplistically assume that the flux number counts of both populations has the *rather steep* power-law index of $\alpha = -2$, to emphasize the effect. The labelled thin blue curve in the top panel is the BigBOSS case with just the diagonal Schur-Limber estimator.

$\approx -0.05(\alpha + 1)$ per cent bias that is roughly constant with z_i . In addition, Eq. (61) shows that if $N_i^{(p)}$ is well below the peak in i , this bias can be particularly severe.

Fig. 11 illustrates the importance of magnification bias for a case in which the photometric sample consists of all galaxies with $i^{(p)} < 25.3$ and different spectroscopic samples, all covering $0 < z < 2.5$. (Lower redshift samples would be less biased by magnification.) For simplicity, we take $\alpha_i^{(x)} = -2$ for all populations, which emphasizes the effect (being characteristic of the bright end of quasar counts; fainter quasars have slope $\alpha \sim -0.5$; Bartelmann & Schneider 2001; Scranton et al. 2005, and the faint-end slope for galaxies is $-(0.5 - 1)$; Bouwens et al. 2012). The thick blue curves represent BigBOSS and 10^4 deg^2 , the black curves a survey with $dN^{(s)}/dz = 10 \text{ deg}^{-2}$ over 10^4 deg^2 , and the red curves a survey with $i^{(s)} = 23$ and 40 deg^2 . Solid (dashed) curves indicate that the bias results in an overestimate (underestimate). The top panel is the bias relative to $N_i^{(p)}$, and the bottom panel is this relative to the fractional error. At $z < 1.5$, the bias is ~ 1 standard deviation for two of the cases. However, for BigBOSS (which has fractional errors of

$\sim 10^{-2}$), the bias is 10σ over many of the redshift bins of interest. For all the cases, the biases are largest at $z < 0.5$ and $z > 1.5$, redshifts at which there is a significant fall off in the photometric population. The fact that these curves can become negative contrasts with the Schur-Limber estimator, which would always be biased high. The thin blue curves are the Schur-Limber estimator for the case with BigBOSS. We find that the bias of the Schur-Limber estimator (Eq. 61) is typically larger than the bias of the full minimum variance quadratic estimator (that ignores magnification).

In all cases magnification bias can be computed given an estimate for the $\alpha_i^{(x)}$ and removed. The main issue is uncertainty in the $\alpha_i^{(x)}$. It should be reasonably straightforward to remove the bias at redshifts greater than the peak in $dN^{(p)}/dz$ (where it is most severe) as the spectroscopic galaxies act as the sources and their $\alpha_i^{(s)}$ is easily measured. However, uncertainty in $\alpha_i^{(x)}$ could be the limiting factor in $N_i^{(p)}$ constraints at redshifts where the photometric galaxies act as the source, particularly in surveys that can place percent-level errors on the $N_i^{(p)}$ and that extend to high redshifts. In such cases, the error will be approximately set by the fractional bias of $N_i^{(p)}$ owing to magnification (what is plotted in Fig. 11) times the fractional uncertainty in $\alpha^{(x)}$. Knowledge of $\alpha^{(x)}$ to $10|\alpha^{(x)} + 1|$ per cent precision is required for this not to be the limiting factor for the BigBOSS case considered above. Since magnification only depends on the sources' N_i and not their b_i , the significant bias of BigBOSS also suggests that it can use magnification to break this degeneracy and separately estimate the $b_i^{(p)}$ to $10|\alpha^{(x)} + 1|$ per cent precision. We revisit the impact of magnification in Section 7, showing that is less onerous in the cases of (1) photo- z calibration and (2) estimating the redshift distribution of diffuse backgrounds.

Analogous to magnification, intervening dust can also correlate background galaxies with foreground ones for surveys in the optical and bluer wavelengths (Ménard et al. 2010). At linear scales, this effect will induce correlations that are a biased tracer of the projected density. The magnitude of this effect with redshift could be determined with multi-band photometry using a population with uniform spectra, e.g. quasars, and this information would allow it to be corrected for in cross correlation studies again to the extent that the $\alpha_i^{(x)}$ are known.

7 CALIBRATING PHOTOMETRIC REDSHIFTS AND CLEANING CORRELATED ANISOTROPIES FROM MAPS

Our previous results can be generalized to spectroscopically calibrate the dN/dz of a photometric population that is partitioned by photometric redshift, an application which is relevant for large-scale clustering and weak lensing analyses on photometric populations. When the catastrophic failure rate of the photometric redshift estimate is small, then it may be fruitful to self-calibrate by internal cross-correlations between different photometric redshift bins. However, if the catastrophic failure rate is large, there can be large degeneracies in the reconstruction from self calibrations, and it will be more robust to calibrate photometric redshifts with

a spectroscopic sample. In Section 7.1, we discuss the latter, and Section 7.2 discusses the former. This section also addresses the more general problem of estimating the redshift distribution of a photometric sample in which other constraints exist for the sample's redshift distribution. Finally, in Section 7.3 we discuss how our results can be used to statistically clean diffuse background maps.

7.1 Spectroscopic calibration

Consider binning the photometric sample by some property that we refer to as its “photo- z ”, and we denote the sample in photometric redshift bin ‘ m ’ as ‘ pm ’. One can think of m as, for example, indexing a probability distribution of the sample's redshift as estimated from photometry. The goal is to use cross-correlations with a spectroscopic sample to constrain this probability distribution. The primary difference with the calculations in prior sections and this calculation is that the fluctuations from each photometric redshift bin are more likely localized in redshift than the full photometric sample. (We defer discussion of internal correlations between different photo- z bins to Section 7.2.)

If this is the case, our approximate formulae for the sensitivities in different limits (Eqs. 44, 45, and 46) are altered so that $f_i \approx N_i^{(pm)}/N_{\text{tot}}^{(pm)}$ and $\beta_i \approx [T_i^{(pm)}]^2/[T_{\text{tot}}^{(pm)}]^2$, where $N_i^{(pm)}$ [$b_i^{(pm)}$] is the sky density [linear bias] of the photometric galaxies in redshift bin m that are actually at redshift i , $N_{\text{tot}}^{(pm)} \equiv \sum_i N_i^{(pm)}$, $T_i^{(pm)} \equiv D_i b_i^{(pm)} N_i^{(pm)}$, and $T_{\text{tot}}^{(pm)} \equiv (\sum_i [T_i^{(pm)}]^2)^{1/2}$. These relations for f_i and β_i are exact in the distant observer approximation. With these replacements, we can recast our formulae in the rare and abundant limits for the case of photo- z calibration.

If the spectroscopic sample is in the rare limit, the potential constraint on the population in photo- z bin m that is actually in redshift bin i follows from Eq. (45) and is

$$\frac{\delta T_i^{(pm)}}{T_{\text{tot}}^{(pm)}} \approx \frac{0.06}{b_i^{(s)} D_i} \left(\frac{N_i^{(s)}}{10^4} \right)^{-1/2} \left(\frac{1+z}{2} \right)^{-0.5}. \quad (62)$$

Note that $\delta T_i^{(pm)}/T_{\text{tot}}^{(pm)}$ equals the outlier fraction for bin $i \neq m$ in the limit that pm primarily falls in redshift bin m and that the clustering is redshift independent. For pm to be in the dense galaxy limit (as Eq. 62 assumes) requires that the redshift span of the photo- z bin is sufficiently concentrated that $\sum_i [D_i b_i^{(pm)}]^2 C_{ii} > [N_{\text{tot}}^{(pm)}]^{-1}$, which roughly should hold if $dN^{(pm)}/dz$ at the full width half maximum is greater than $[dN^{(p)}/dz]_{-2}^{\text{crit}}$.

In the contrasting case of a dense spectroscopic and photometric sample, it follows from Eq. (42) that

$$\frac{\delta T_i^{(pm)}}{T_{\text{tot}}^{(pm)}} \approx 0.03 \left(\frac{f_{\text{sky}}}{0.001} \right)^{-1/2} \left(\frac{\ell_0}{10^3} \right)^{-1}. \quad (63)$$

Eqs. (62) and (63) demonstrate that cross-correlations can be used to constrain the fractional number (times bias) from pm in bin i at the part in a hundred level with $10^5 - 10^6$ spectra per unit redshift (for rare spectra) or $f_{\text{sky}} = 10^{-3}$ (for high spectral densities).

Fig. 12 presents estimates for how well the redshift distribution of a photo- z bin can be reconstructed in bins of size $\Delta z = 0.05$ with cross-correlations for the $z_m = 1.45$ photo- z bin, assuming the “outlier” photo- z 's that are not

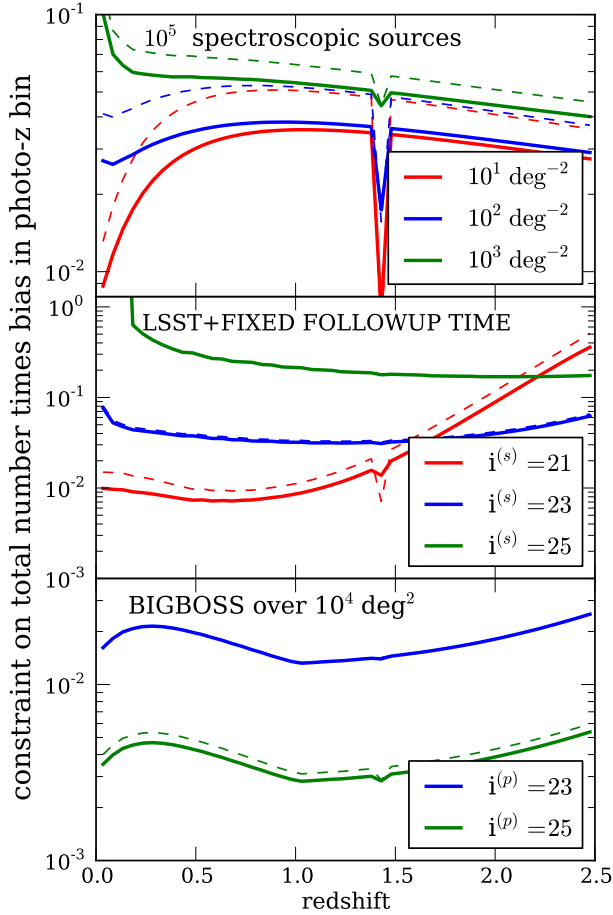


Figure 12. Estimates for how well the redshift distribution of sources (times their bias) in the photo- z bin pm can be reconstructed with cross-correlations, assuming redshift bins of size $\Delta z = 0.05$. Our calculations assume that much of pm resides in the $z_m = 1.45$ bin, with “outlier” galaxies distributed uniformly in the range $0 < z < 2.5$, and that the number density at z_m is that of a survey complete to $i^{(p)} = 25.3$ unless specified otherwise. The solid curves assume half of the galaxies in this photo- z bin reside outside of it, uniformly distributed so that $N_i^{(pm)}/N_{\text{tot}}^{(pm)} = 10^{-2}$ for $i \neq m$. The dashed curves are the same but for an outlier fraction of $N_i^{(pm)}/N_{\text{tot}}^{(pm)} = 10^{-3}$ (so that most galaxies reside at z_m). The top panel shows the constraints from different spectroscopic samples with the specified constant $dN^{(s)}/dz$ over $0 < z < 2.5$ and with f_{sky} adjusted so that there are 10^5 total spectra. The middle panel shows three different spectroscopic samples that could be obtained for the same total telescope time (with the same specifications as in the top panel in Fig. 9). The bottom panel is for a spectroscopic sample with the specifications of BigBOSS and the specified limiting photometric magnitudes. All curves truncate the summation over ℓ at ℓ_{NL} .

actually at the redshift z_m are distributed uniformly in the range $0 < z < 2.5$. The solid curves assume half of the galaxies in this photo- z bin reside outside of it, uniformly distributed over i bins so that $N_i^{(pm)}/N_{\text{tot}}^{(pm)} = 10^{-2}$ for $i \neq m$. The dashed curves are the same but for an outlier fraction of $N_i^{(pm)}/N_{\text{tot}}^{(pm)} = 10^{-3}$ so that only 5 per cent of galaxies reside outside the photo- z bin z_m . The top panel shows the constraints from different spectroscopic samples

with the specified $dN^{(s)}/dz$, which is held constant over $0 < z < 2.5$ and for fixed total number of spectra. This panel shows that Eq. (62) is in qualitative agreement with these estimates, noting that here $N^{(s)} = 4 \times 10^4$. (We discuss the dip at $z_m = 1.45$ below.) Especially for the two lower number densities, the constraint depends weakly on the density of spectra as Eq. (62) predicts.

The middle panel in Fig. 12 is for the photometric sample with the specifications of the LSST gold sample ($i^{(p)} = 25.3$) and for different spectroscopic samples that could be obtained for the same total telescope time (with the same specifications as in the top panel in Fig. 9). In this case, both the photometric and spectroscopic galaxies are at least marginally in the dense limit such that Eq. (63) applies, and the sensitivity scales roughly as $f_{\text{sky}}^{1/2}$. In the three cases plotted, f_{sky} equals 2.5×10^{-4} , 10^{-3} , and 4×10^{-2} . The predictions in this panel depend weakly on the outlier fraction (compare the solid and dashed curves, which in two of the cases lie on top of each other). The sensitivity of followup to $i^{(s)} = 21$ also falls off substantially at the highest redshift, which reflects that the spectroscopic galaxies are entering the rare regime.

The bottom panel shows the case of a spectroscopic sample with the specifications of BigBOSS and the specified limiting photometric magnitudes, and that the surveys’ overlap is 10^4 deg^2 . The BigBOSS sample is on the borderline of the rare limit (especially at the lowest and highest z) such that this panel is most difficult to relate to our predictions. The rare-abundant limit given by Eq. (62) appears to apply since BigBOSS has $N_i^{(s)} \sim 10^7$ at $z \sim 1$ for the case of $i^{(pm)} = 25$ (Fig. 1). However, it does not hold for the $i^{(pm)} = 23$ case, as $i^{(pm)} = 23$ is also on the borderline of being in the rare limit with $dN^{(pm)}/dz = 5,000 \text{ deg}^{-2}$ at z_m , which results in a loss in sensitivity compared to $i^{(pm)} = 25$.

Auto-correlations (which were dropped in the derivations that led to Eqs. 62 and 63) add additional information. We find that auto correlation estimates add little extra information for redshift bins that contain only a small fraction of pm galaxies. However, for the redshifts that contain the bulk of pm , they can improve the constraint by an order of magnitude. This can be seen by focusing in on the dip at $z_m = 1.45$ in Fig. 12, which corresponds to the redshift that contains half or more of the galaxies. Eqs. (62) and (63) do not predict a dip. Especially with a rare spectroscopic sample as investigated in the top panel (where the cross-correlations can be quite noisy) and a low outlier fraction, much of the constraint on the number at z_m owes to the large value of \widehat{pm}^2 , which indicates many galaxies are concentrated in a narrow range in redshift.

Eqs. (62) and (63) [and Fig. 12] show that a 0.0015 error on the fractional number on ‘all outlying peaks’ in the true redshift distribution of pm would be difficult to achieve with spectroscopic cross-correlations (even ignoring that the $b_i^{(p)}$ also need to be constrained to $\mathcal{O}(10^{-3} f_c^{-1})$, where f_c is the contamination fraction). Such sensitivity is required for uncertainty in the redshift distribution of the lenses to not to be the limiting factor for the next generation of photometric weak lensing surveys (Bernstein & Huterer 2010). These issues aside, the case of BigBOSS cross-correlations with a photometric sample complete to $i^{(p)} = 25$ over 10^4 deg^2 (green curves in bottom panel of Fig. 12) achieves an error

that is comparable to the Bernstein & Huterer (2010) requirement. To quantitatively answer the question of whether a BigBOSS-like survey is sufficient for futuristic weak lensing surveys requires an analysis of the bias on cosmological parameters induced by the pattern of uncertainties we find.

Thus far we have ignored prior information on the redshift distribution of the photo- z subsample pm . Often it is the case that we have prior information on the distribution of $N_i^{(pm)}$, e.g. from the photometric redshift PDF per galaxy (Lima et al. 2008; Freeman et al. 2009; Sheth & Rossi 2010). In this case our formalism has only minor modifications. Appendix A2 reviews how the quadratic estimator formalism generalizes to include prior information. For a Gaussian prior on the N_i (dropping pm superscripts for simplicity), the estimator with a prior becomes

$$\hat{N}_i = [\hat{N}_i]_{\text{last}} + [\mathbf{F} + \mathbf{F}_P]_{ij}^{-1} \left\{ \sum_{\ell, m} \left[\begin{pmatrix} \hat{p} & \hat{s} \end{pmatrix} \mathbf{Q}_j \begin{pmatrix} \hat{p} \\ \hat{s} \end{pmatrix} \right. \right. \\ \left. \left. - \text{Tr}[\mathbf{A}^{-1} \mathbf{A}_{,j}] \right] + [\mathbf{F}_P]_{jk} \left(N_{P,k} - [\hat{N}_k]_{\text{last}} \right) \right\}, \quad (64)$$

where \mathbf{F}_P and $N_{P,i}$ are respectively the inverse covariance matrix and mean of the prior. The prior pulls the estimated quantity towards $N_{P,k}$, and this pull dominates if the prior is more peaked than the likelihood of the data.

The final subtlety we address with regard to photo- z calibration is cosmic magnification. Section 6 showed that cosmic magnification can be a significant bias if unaccounted for redshift estimation of the entire photometric sample. Magnification is less onerous for photo- z calibration to the extent that the redshifts of the photo- z samples are constrained. Appendix C2 addresses how magnification can be accounted for in this case.

7.2 Self calibration of photometric sample

Self-calibration of redshifts by cross correlating different photo- z bins within a photometric sample has the potential to achieve a tighter constraint on the $N_i^{(pm)}$ than calibration using correlations with spectroscopically identified galaxies, since spectroscopic samples are likely to either be sparser in number or distributed over narrower fields than photometric ones. Self-calibration of a photometric survey with cross-correlations has been investigated in several studies (Huterer et al. 2006; Schneider et al. 2006; Benjamin et al. 2010). Here we show that the maximum sensitivity to $dN^{(pm)}/dz$ that can be achieved with photometric self-calibrations is strikingly similar to the previously considered case of abundant spectroscopic and photometric samples.

For self-calibration to be successful, the redshift distribution of the photometric sample pm needs to be much better known than in the case of calibration with spectroscopic cross-correlations. This is because the redshift of pn for all n is the only knowledge one has to measure the redshift of pm : If pn is not centered around a single redshift, it is unclear how finite $\langle \hat{p} \hat{m} \rangle$ translates into the redshift distribution of sample pm . To avoid this difficulty, we assume that most of sample pm falls into redshift bin z_m . This assumption is the best case scenario, and will allow us to put a lower bound on

the constraint from self calibrations.¹⁷ Thus, the covariance matrix of the the different photo- z bins is

$$B_{mn} \equiv \langle p^{(m)} p^{(n)} \rangle = \sum_{ij} T_i^{(pm)} T_j^{(pn)} C_{ij} + w_{ii}^{(pm pn)} \delta_{ij}^K, \\ \approx \sum_{i=m,n} T_i^{(pm)} T_i^{(pn)} C_{ii} + w_{ii}^{(pm pn)}, \quad (65)$$

and we have assumed the same discretization in redshift to specify both the photometric and actual redshift bins. In the second line, the sum is evaluated at only one value of i if $m = n$ (i.e. the auto-correlation). The approximate equality in the last line follows from assuming C_{ij} is diagonal (as holds in the Limber approximation), that $T_m^{(pm)} \equiv D_m b_m^{(pm)} N_m^{(pm)} \gg \sum_{i \neq m} T_i^{(pm)}$, and from keeping terms that are $\mathcal{O}(T_i^{(pm)}/T_m^{(pm)})$ or larger. This is the limit in which the fraction of catastrophic photo- z 's is small and where the covariance matrix B_{mn} is diagonally dominated. In this limit, and to lowest order in $\alpha_{m,i} \equiv T_i^{(pm)}/T_m^{(pm)}$, the Fisher matrix with respect to the $T^{(pm)}$ is

$$\mathbf{F}_{T_n^{(pm)} T_m^{(pn)}} \approx \sum_{\ell, m} \left(\frac{T_n^{(pn)} C_{nn} T_m^{(pm)} C_{mm}}{B_{mm} B_{nn}} \right), \quad (66)$$

where $B_{nn} \approx [T_n^{(pn)}]^2 C_{nn} + w_{nn}^{(pn pn)}$, and the matrix is zero between other combinations of parameters. The quadratic estimator for $T_n^{(pm)}$ in this limit can also easily be written as it only involves correlations between the photometric samples m and n . Thus, in the diagonally dominated limit, the parameter $T_n^{(pm)}$ only correlates with $T_m^{(pn)}$, and there is a perfect degeneracy that must be broken by adding a prior (often catastrophic errors occur in one redshift direction) or going to higher order terms that are suppressed by another factor of $\alpha_{m,i}$. In the case of the prior that constraints $T_m^{(pn)}$ to be zero, many of our previous results hold as Eq. (66) is the same as Eq. (35) and its other incarnation in Eq. (42) with the replacement $\beta(z) = 1$ and a slightly different number dependence. (In fact, we do not need the additional approximation of $S = 1$, as was made there.) Thus, if $T_n^{(pn)} \gg 10^4 b^{-2} \Delta z \text{ deg}^{-2}$, so that the abundant limit holds,

$$\frac{\delta T_n^{(pm)}}{T_m^{(pm)}} \approx 10^{-3} f_{\text{sky}}^{-1/2} \left(\frac{\ell_0}{10^3} \right)^{-1}. \quad (67)$$

Photometric self-calibration over a significant fraction of the sky is capable of part in 10^3 accuracy required by the next generation of weak lensing surveys (e.g., Bernstein & Huterer 2010), but with the same caveat as noted in the previous subsection that we have not calculated the bias on cosmological parameters. In addition, this error only applies to the case of a single catastrophic error direction. If the latter does not hold, the constraint is likely to be weakened by the factor $\sqrt{\alpha_{m,i}}$. This conclusion would be improved somewhat if neighboring photo- z bins had significant overlap in redshift so that some of the $\sqrt{\alpha_{m,i}}$ were not so small.

More generally, the full covariance matrix of the photo- z bins, B_{mn} , (plus overlapping spectroscopic populations)

¹⁷ This assumption requires a highly artificial top hat photo- z distribution at z_m for consistency. However, we expect that our result is more general than this choice.

can be used as the covariance matrix in the minimum variance quadratic estimator. This self-calibration estimator is likely to be more sensitive than the algorithm discussed in Benjamin et al. (2010), the only self-calibration method that we are aware of, as that algorithm uses linear combinations of the $A_{\alpha\beta}$ that encapsulate a subset of the full covariance and does not weight scales optimally.

7.3 Cleaning correlated anisotropies from a map

Our estimator is optimal for *statistically* estimating the level of (and, hence, cleaning) correlated anisotropies from angular cross-correlations between diffuse background/foreground maps and spectroscopic galaxies. The fractional errors we quote on number are equivalent to the error with which anisotropies can be statistically removed. Thus, the survey optimizations for this application are equivalent to those discussed for $N_i^{(p)}$ estimates. Our previous calculations suggest that correlating anisotropies can be cleaned statistically to the 1 per cent level. For wide field observations of diffuse redshifted 21cm emission, this factor of 100 could be helpful if extragalactic sources are found to be a limiting factor.¹⁸ For CMB analyses, cross-correlations could also be interesting for studying the redshift distribution and cleaning of foregrounds. For example, it could better enable the separation of the cosmic infrared background (CIB) from CMB anisotropies generated at higher redshift. (CIB contamination is currently the limiting factor in measurements of kinetic Sunyaev-Zeldovich effect, which conveniently does not correlate with the s_i ; Reichardt et al. 2012). Kashlinsky et al. (2007) investigated correlations on $\sim 10'$ scales between diffuse anisotropies in Spitzer and HST deep fields. Our results suggest the sensitivity to the clustering component would be increased with wider fields (perhaps using shallower ground based observations rather than HST, since we found that the extremely high number density in the HST fields is not useful).

For diffuse anisotropies, gravitational lensing enters at second order because lensing preserves surface brightness. Thus, at large scales its impact on correlating the anisotropies in a map with the spectroscopic sample is small. If the “spectroscopic” sample is measured at sufficiently high redshifts that the magnification-magnification term becomes important, only then can magnification result in a linear order diffuse foreground–spectroscopic population cross-correlation signal. Magnification also has the effect of correlating the \hat{s}_i , which can bias the estimate. However, both magnification effects should be correctable as the $\alpha_i^{(s)}$ can be measured.

8 MOCK SURVEYS

We are interested in understanding the robustness with which the proposed estimator converges to the input $N_i^{(p)}$. To investigate its convergence, mock surveys are generated

¹⁸ It is thought that emission from the Galaxy is more problematic for 21cm measurements, although the contribution of extragalactic sources to the foregrounds increases with ℓ (McQuinn et al. 2006).

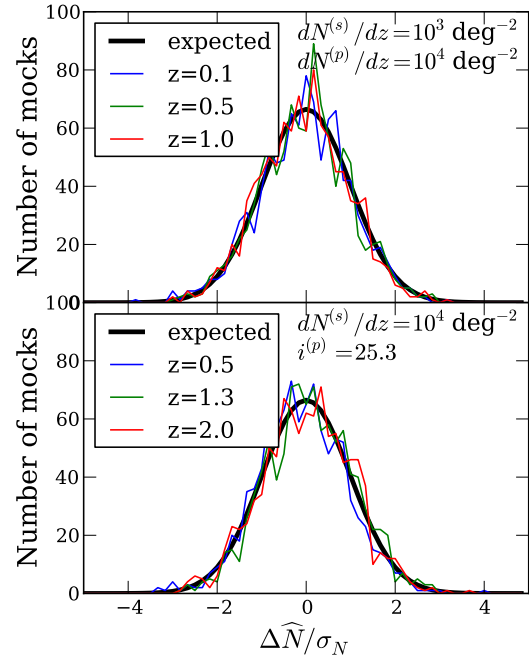


Figure 13. Demonstration of estimator convergence, showing the distribution of estimated value of the estimator in units of the Fisher error for 1,000 mocks. The thick solid curve is the expected distribution of estimates. For each mock, we start off with initial values for the $N_i^{(p)}$ that are each an order of magnitude smaller than their actual value. The top panel shows the case of a $10 \times 10 \text{ deg}^2$ field with the specified populations and 10 bins spanning $0 < z < 1$ (resulting in ~ 10 per cent errors). The bottom is a $30 \times 30 \text{ deg}^2$ field with a photometric sample complete to $i^{(p)} = 25.3$ and 50 bins spanning $0 < z < 2.5$ (resulting in ~ 1 per cent errors). We find that the estimator robustly converges to its minimum, even when it starts far from it, and that in both cases there are zero outliers at $> 5 \sigma$ in the 1,000 mocks.

by decomposing the covariance matrix \mathbf{A} into its eigenvectors \mathbf{e}_α and eigenvalues λ_α for $\alpha \in [0, N_{\text{bin}}]$. Then, a realization of the galaxy field that at multipole ℓ that has this covariance matrix is given by

$$g_\beta(\ell, m) = \sum_{\alpha=0}^{N_{\text{bin}}} r_\alpha \lambda_\alpha(\ell)^{1/2} [\mathbf{e}_\alpha(\ell)]_\beta, \quad (68)$$

where r_α is a Gaussian deviate with unit variance. Here, g_i corresponds to the overdensity in redshift bin i of the spectroscopic survey, and g_0 is the overdensity in the photometric sample. Our mocks assume that we are operating in a small enough patch such that there is a one-to-one mapping between wavevectors and spherical harmonics. In addition, our mocks assume linear theory and the Limber approximation. These approximations should not impact the conclusions per our previous results.¹⁹

¹⁹ These mocks have one significant advantage over a real survey: they are periodic. Hence, we do not have to worry about the survey window functions, and different modes on the lattice are truly independent. We discussed how to deal with these real-world complications in Section 5.3.

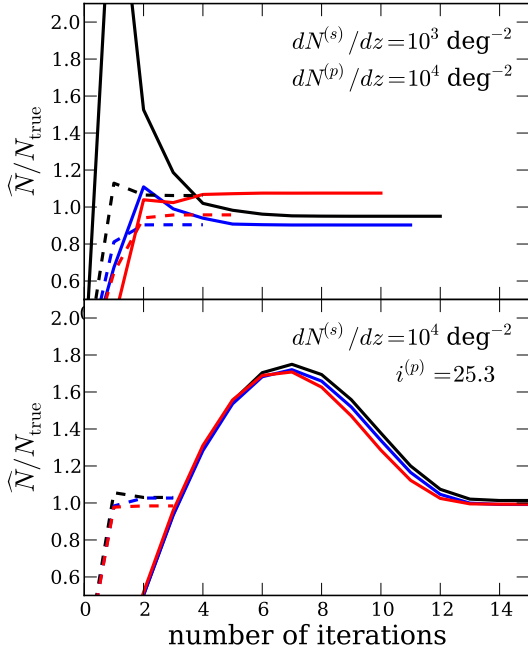


Figure 14. Walk of the estimated N as a function of iteration number in the middle redshift bin for the same two cross-correlation examples as described in Fig. 13 and the text. The solid curves are the full minimum variance estimator, and the dashed curves are the Schur-Limber estimator (which converges more quickly). The curves terminate after the last iteration changed the estimated $\hat{N}_i^{(p)}$ by less than a part in 10^5 when averaged over all i . The initial guesses for the $\hat{N}_i^{(p)}$ are taken to be an order of magnitude too small. The asymptotic value of each $\hat{N}_i^{(p)}$ shown in this figure is within 2σ of the input $N_i^{(p)}$.

We generate 1,000 mocks for two contrasting cases to illustrate the estimator’s performance:

- $10 \times 10 \text{ deg}^2$ field with $dN^{(s)}/dz = 10^3 \text{ deg}^{-2}$, $dN^{(p)}/dz = 10^4 \text{ deg}^{-2}$, and 10 redshift bins spanning $0 < z < 1$ and each with $1,000^2$ pixels, which results in ~ 10 per cent errors on the $\hat{N}_i^{(p)}$,
- $30 \times 30 \text{ deg}^2$ field with $dN^{(s)}/dz = 10^4 \text{ deg}^{-2}$ and photometry up to $i^{(p)} = 25.3$, spanning $0 < z < 2.5$ with 50 bins and 300^2 pixels, which results in ~ 1 per cent errors on the $\hat{N}_i^{(p)}$.

The resolution of each mock is sufficient to resolve the scales that contain the bulk of the information (Section 5.3). Resolving these scales forces these examples to use smaller areas and higher number densities than many of the previous examples to achieve sensitivity to the cross-correlation signal at modest computational expense.

Next, we apply the estimator to the harmonic space realization of these mocks. (It would be equivalent to apply our estimator in real space using the results of Section 5.) Fig. 13 demonstrates that the minimum variance quadratic estimator converges to the expected Gaussian distribution of errors. This holds even though we started with initial estimates for the $\hat{N}_i^{(p)}$ that are an order of magnitude smaller than the true values used in the mocks. There are no outliers from the 5σ regions plotted in this figure for the cases

shown. Thus, our estimator does not tend to find local extrema. We find that only when the Fisher errors become $\mathcal{O}(1)$ does the estimator no longer converge properly in all cases. However, the Schur-Limber estimator in all cases we investigated successfully converged to the expected distribution of estimates. This result is not surprising as the Schur-Limber estimator always minimizes $\sum_{\ell,m} v_i (A_{0i} - \hat{p}s_i)$, with the v_i being weak functions of the other $N_j^{(p)}$. Thus, it is advisable to first use the Schur-Limber estimator in cases in which the $\hat{N}_i^{(p)}$ are poorly constrained (and often in this limit the Schur-Limber estimator will in fact be optimal).

Fig. 14 shows the walk of the $\hat{N}_{N_{\text{bin}}/2}^{(p)}$ estimate as a function of iteration number for the middle redshift bin in the two cross-correlation cases. The solid curves are the full minimum variance estimator, and the dashed curves are the Schur-Limber estimator (which converges more quickly). The curves terminate when the next successive iteration changes the estimated $\hat{N}_i^{(p)}$ by less than a part in 10^5 when averaged over all i . The Schur-Limber estimator converges rapidly in both examples (after 3–4 iterations). This similar convergence rate is despite the two cross-correlation cases being considerably different in terms of their sensitivity, their $dN^{(p)}/dz$, and their N_{bin} . For the minimum variance quadratic estimator, convergence requires additional steps – as many as 20 iterations for the case in the bottom panel.

9 BREAKING THE BIAS – NUMBER DEGENERACY

Much of our discussion has ignored that cross-correlations do not constrain number alone but instead bias times number.²⁰ For many applications, bias times number is in fact the quantity of interest, including attempts to measure 3D correlations with angular correlations or attempts to subtract correlated anisotropies from a map of diffuse backgrounds. However, knowing the bias is particularly important to the application of calibrating the lens redshifts for weak lensing. RSDs as well as lensing magnification formally provide terms that break the bias–number degeneracy. However, we argued that breaking this degeneracy is unlikely with RSDs. Cosmic magnification is more promising: We argued that surveys capable of percent-level $N_i^{(p)}$ determinations may be able to constrain the bias to 10 per cent.

Other possibilities for breaking this degeneracy require using additional scales or constraints not included in our earlier estimates. Such methods to break this degeneracy include modeling of the one-halo term in $\langle ps_i \rangle$; abundance matching or other modeling methods to map galaxy number to bias (e.g. Conroy et al. 2006, as $b_i^{(p)}$ is a weak function of mass for abundant halos); galaxy-galaxy lensing with the photometric galaxies as both sources and lenses (using the $b_i^{(p)} N_i^{(p)}$ from cross-correlation measurements – the quantity

²⁰ The bias often can be parametrized as a smoothly and slowly varying function with redshift. An exception is samples with hard color cuts, where the underlying galaxy population, and hence the large-scale bias, can change relatively quickly with z at points where spectral features transition in and out of filters. In such cases, knowledge of $b_i^{(p)} N_i^{(p)}$ is more difficult to translate into knowledge about $N_i^{(p)}$.

needed for the lenses – to constrain $dN^{(p)}/dz$ of the sources); and measurements of the 2nd order bias, either in the two point function or higher order statistics. While several of these avenues appear promising, we shall not pursue them here.

10 CONCLUSIONS

Determining the redshift distribution of a particular population of astronomical objects is often quite difficult. However, since most cosmological objects are clustered (i.e., they trace the same matter field on large scales), objects that are close together on the sky are also likely to be close together in redshift. Thus, the redshift distribution of a population of objects can be determined by cross-correlating it in angle with a population whose redshift distribution is better known. This paper presented a new, optimal estimator for the redshift distribution of a given population in terms of cross-correlations. We found that this estimator (1) is quite intuitive in a number of limits, (2) is straightforward to apply to observations, (3) robustly finds the posterior maximum, and (4) conveniently selects angular scales at which the fluctuations are well approximated as independent between redshift bins and at which linear theory applies. In addition, we provided analytic formulae that can be used to quickly estimate the sensitivity of cross-correlations between overlapping surveys to $b dN/dz$ – the linear bias times angular number density per redshift. We compared our estimator to others suggested in the literature, showing that it produces considerably smaller errors than the familiar estimator of Newman (2008).

The optimal estimator’s fractional error on the number of objects (times their bias) in a redshift bin scales as $\sqrt{10^2 N'_{\text{bin}} / \mathcal{N}^{(s)}}$ if the spectroscopic sample has a mean angular density of less than a few thousand and the unknown sample has a mean density larger than this value. Here, $\mathcal{N}^{(s)}$ is the total number of spectra per unit redshift, and N'_{bin} is the number of redshift bins spanned by the bulk of the unknown population.²¹ Thus, it is not necessarily better to use a narrow, deep spectroscopic survey covering tens of degrees than a wide, shallow one. Once the spectroscopic and unknown populations have $dN/dz \gg 10^4 b^{-2} \text{ deg}^{-2}$, the sensitivity scales simply with the fraction of sky covered (again with an intuitive formula) and no longer depends on just the total number of spectra. We found that upcoming spectroscopic surveys that aim for millions of spectra can potentially achieve percent-level constraints on the $b dN/dz$ of an unconstrained population. Furthermore, we showed that our estimates for the constraints on $b dN/dz$ also apply to spectroscopically calibrating samples binned by their photometric redshift, and we also commented on the sensitivity of photometric self-calibration. We found that cross correlations with upcoming large spectroscopic data sets may be

²¹ This formula is analogous to the sensitivity of direct spectroscopic followup to dN/dz , where the error is the square root of the number of spectra in a redshift bin. It indicates that cross correlations have an order of magnitude larger error at fixed number of spectra. However, cross correlations have the significant advantage of not requiring the spectra to be of the same objects for which the redshift distribution is desired.

able to achieve the stringent source redshift calibration requirements of future weak lensing surveys, but further modeling is required to quantify this.

We investigated a number of approximations and how they bias the estimator. In the Limber approximation – which we found to be excellent – the covariance matrix for this problem can be analytically inverted, allowing simple expressions for the estimator. We showed that the nearly optimal, Limber-approximation estimator can be expressed as an iteration of

$$\hat{N}_i = [\hat{N}_i]_{\text{last}} + \sum v_i (\hat{p} \hat{s}_i - \langle \hat{p} \hat{s}_i \rangle) / \sum v_i \frac{d\langle \hat{p} \hat{s}_i \rangle}{dN_i}, \quad (69)$$

where the v_i are weights comprised of intuitive combinations of the covariance matrix (Eq. 53) and $\hat{p} \hat{s}_i$ is the cross-correlation between the unknown sample and the spectroscopic sample in bin z_i . The summations are either evaluated over bins in angular separation or spherical harmonic indices depending on whether $\hat{p} \hat{s}_i$ is measured in configuration or harmonic space. Furthermore, we found that the bias from assuming the Limber approximation was minute and also argued that the same holds for redshift space distortions. We found that cosmic magnification can be a significant source of estimator bias, becoming important once surveys achieve $\lesssim 10$ per cent statistical errors (especially if the surveys extend to $z \gtrsim 2$ or if dN/dz of the unknown sample falls off quickly). We discussed strategies for correcting this bias. This bias is easy to correct for the case in which the unknown population has photo- z estimates or in which the magnification bias comes from the unknown population acting as the lens (which is the scenario that leads to the largest bias).

The techniques developed in this paper can be applied to a wide range of existing and upcoming surveys from DES, GAMA and WISE, to LSST, Euclid and the SKA. We intend to apply this estimator to observational data in a future paper.

MM acknowledges support by the National Aeronautics and Space Administration through Hubble Postdoctoral Fellowship awarded by the Space Telescope Science Institute, which is operated by the Association of Universities for Research in Astronomy, Inc., for NASA, under contract NAS 5-26555. MW is supported by NASA.

REFERENCES

- Abramowitz M., Stegun I. A., 1972, Handbook of Mathematical Functions
- Bartelmann M., Schneider P., 2001, *physrep*, 340, 291
- Benjamin J., et al., 2012, *ArXiv:1212.3327*
- Benjamin J., van Waerbeke L., Ménard B., Kilbinger M., 2010, *MNRAS*, 408, 1168
- Bernstein G., Huterer D., 2010, *MNRAS*, 401, 1399
- Bernstein G. M., 1994, *ApJ*, 424, 569
- Bond J. R., Jaffe A. H., Knox L., 1998, *PRD*, 57, 2117
- Bouwens R. J., Illingworth G. D., Oesch P. A., Trenti M., Labbé I., Franx M., Stiavelli M., Carollo C. M., van Dokkum P., Magee D., 2012, *ApJL*, 752, L5
- Brainerd T. G., Blandford R. D., Smail I., 1996, *ApJ*, 466, 623

- Christensen N., Meyer R., Knox L., Luey B., 2001, *Classical and Quantum Gravity*, 18, 2677
- Colless M., Dalton G., Maddox S., Sutherland W., Norberg P., Taylor K., 2001, *MNRAS*, 328, 1039
- Conroy C., Wechsler R. H., Kravtsov A. V., 2006, *ApJ*, 647, 201
- Cooray A., Sheth R., 2002, *physrep*, 372, 1
- Corbató F. J., Uretsky J. L., 1959, *J. ACM*, 6, 366
- Cunha C. E., Lima M., Oyaizu H., Frieman J., Lin H., 2009, *MNRAS*, 396, 2379
- Dawson K. S., et al., 2013, *AJ*, 145, 10
- Dodelson S., 2003, *Modern Cosmology*
- Drinkwater M. J., Jurek R. J., Blake C., Woods D., Pimblet K. A., Glazebrook K., Sharp R., Small T., Wisnioski E., Wyder T., Yee H. K. C., 2010, *MNRAS*, 401, 1429
- Driver S. P., Hill D. T., Kelvin L. S., Robotham A. S. G., Liske J., Norberg P., Baldry I. K., Bamford S. P., Hopkins A. M., Loveday J., Peacock J. A., Andrae E., 2011, *MNRAS*, 413, 971
- Duffy A. R., Meyer M. J., Staveley-Smith L., Bernyk M., Croton D. J., Koribalski B. S., Gerstmann D., Westerlund S., 2012, *MNRAS*, 426, 3385
- Efstathiou G., 2004, *MNRAS*, 349, 603
- Efstathiou G., Bernstein G., Tyson J. A., Katz N., Guhathakurta P., 1991, *ApJL*, 380, L47
- Eisenstein D. J., et al., 2001, *AJ*, 122, 2267
- Eisenstein D. J., Hu W., 1998, *ApJ*, 496, 605
- Erben T., Hildebrandt H., Lerchster M., Hudelot P., Benjamin J., van Waerbeke L., Schrabback T., Brimiouille F., Cordes O., Dietrich J. P., Holhjem K., Schirmer M., Schneider P., 2009, *A&A*, 493, 1197
- Feldman H. A., Kaiser N., Peacock J. A., 1994, *ApJ*, 426, 23
- Freeman P. E., Newman J. A., Lee A. B., Richards J. W., Schafer C. M., 2009, *MNRAS*, 398, 2012
- Fugmann W., 1988, *A&A*, 204, 73
- Gillman E., Fiebig H. R., 1988, *Comput. Phys.*, 2, 62
- Hamaus N., Seljak U., Desjacques V., Smith R. E., Baldauf T., 2010, *PRD*, 82, 043515
- Hamilton A. J. S., 1992, *ApJL*, 385, L5
- Hamilton A. J. S., 1993, *ApJ*, 417, 19
- Hansen F. K., Górski K. M., Hivon E., 2002, *MNRAS*, 336, 1304
- Hildebrandt H., et al., 2012, *MNRAS*, 421, 2355
- Hill G. J., et al., 2008, in Kodama T., Yamada T., Aoki K., eds, *Panoramic Views of Galaxy Formation and Evolution Vol. 399 of Astronomical Society of the Pacific Conference Series, The Hobby-Eberly Telescope Dark Energy Experiment (HETDEX): Description and Early Pilot Survey Results*. p. 115
- Hivon E., Górski K. M., Netterfield C. B., Crill B. P., Prunet S., Hansen F., 2002, *ApJ*, 567, 2
- Hoekstra H., Mellier Y., van Waerbeke L., Semboloni E., Fu L., Hudson M. J., Parker L. C., Tereno I., Benabed K., 2006, *ApJ*, 647, 116
- Hui L., Gaztañaga E., Loverde M., 2007, *PRD*, 76, 103502
- Hui L., Gaztañaga E., Loverde M., 2008, *PRD*, 77, 063526
- Huterer D., Takada M., Bernstein G., Jain B., 2006, *MNRAS*, 366, 101
- Johnston S., et al., 2008, *Experimental Astronomy*, 22, 151
- Jungman G., Kamionkowski M., Kosowsky A., Spergel D. N., 1996, *PRD*, 54, 1332
- Kaiser N., 1987, *MNRAS*, 227, 1
- Kaiser N., 1992, *ApJ*, 388, 272
- Kashlinsky A., Arendt R. G., Mather J., Moseley S. H., 2007, *ApJL*, 666, L1
- Knox L., 1997, *ApJ*, 480, 72
- Kochanek C. S., Eisenstein D. J., Cool R. J., Caldwell N., Assef R. J., Jannuzi B. T., Jones C., Murray S. S., Stern D., 2012, *ApJS*, 200, 8
- Landy S. D., Szalay A. S., 1993, *ApJ*, 412, 64
- Larson D., et al., 2011, *ApJS*, 192, 16
- Lawrence A., Rowan-Robinson M., Ellis R. S., Frenk C. S., Efstathiou G., Kaiser N., Saunders W., Parry I. R., Xiaoyang X., Crawford J., 1999, *MNRAS*, 308, 897
- Le Fèvre O., Vettolani G., Garilli B., Tresse L., Bottini D., Le Brun V., Maccagni D., Picat J. P., Scaramella R., 2005, *A&A*, 439, 845
- Lilly S. J., et al., 2007, *ApJS*, 172, 70
- Lima M., Cunha C. E., Oyaizu H., Frieman J., Lin H., Sheldon E. S., 2008, *MNRAS*, 390, 118
- Limber D. N., 1953, *ApJ*, 117, 134
- Limber D. N., 1954, *ApJ*, 119, 655
- LSST Science Collaboration Abell P. A., Allison J., Anderson S. F., Andrew J. R., Angel J. R. P., Armus L., Arnett D., Asztalos S. J., Axelrod T. S., et al. 2009, *ArXiv:0912.0201*
- Lucas S., 1995, *Journal of Computational and Applied Mathematics*, 64, 269
- Mandelbaum R., et al., 2008, *MNRAS*, 386, 781
- Matthews D. J., Newman J. A., 2010, *ApJ*, 721, 456
- Matthews D. J., Newman J. A., 2012, *ApJ*, 745, 180
- McQuinn M., Zahn O., Zaldarriaga M., Hernquist L., Furlanetto S. R., 2006, *ApJ*, 653, 815
- Ménard B., Scranton R., Fukugita M., Richards G., 2010, *MNRAS*, 405, 1025
- Miller J., 1952, *British Association for the Advancement of Science, Mathematical Tables, Vol. X, Bessel Functions, Part II*
- Narayan R., 1989, *ApJL*, 339, L53
- Newman J. A., 2008, *ApJ*, 684, 88
- Newman J. A., et al., 2012, *ArXiv:1203.3192*
- Nock K., Percival W. J., Ross A. J., 2010, *MNRAS*, 407, 520
- Padmanabhan N., et al., 2007, *MNRAS*, 378, 852
- Pápai P., Szapudi I., 2008, *MNRAS*, 389, 292
- Park C., Vogeley M. S., Geller M. J., Huchra J. P., 1994, *ApJ*, 431, 569
- Peacock J. A., Dodds S. J., 1996, *MNRAS*, 280, L19
- Peacock J. A., Nicholson D., 1991, *MNRAS*, 253, 307
- Peebles P. J. E., 1980, *The large-scale structure of the universe*
- Petersen K. B., Pedersen M. S., 2008, *The Matrix Cookbook*
- Phillipps S., 1985, *MNRAS*, 212, 657
- Phillipps S., Shanks T., 1987, *MNRAS*, 227, 115
- Poularikas A., 2000, *The Transforms and Applications Handbook*
- Rawlings S., Abdalla F. B., Bridle S. L., Blake C. A., Baugh C. M., Greenhill L. J., van der Hulst J. M., 2004, *NAR*, 48, 1013
- Reichardt C. L., et al., 2012, *ApJ*, 755, 70
- Ross N. P., et al., 2009, *ApJ*, 697, 1634
- Schlegel D., et al., 2011, *ArXiv e-prints*

- Schneider D. P., et al., 2010, *AJ*, 139, 2360
- Schneider M., Knox L., Zhan H., Connolly A., 2006, *ApJ*, 651, 14
- Schulz A. E., 2010, *ApJ*, 724, 1305
- Scott D., Srednicki M., White M., 1994, *ApJL*, 421, L5
- Scranton R., et al., 2005, *ApJ*, 633, 589
- SDSS-III Collaboration : Ahn C. P., Alexandroff R., Al-
lende Prieto C., Anderson S. F., Anderton T., An-
drews B. H., Bailey É. A. S., Barnes R., et al. 2012a,
ArXiv:1207.7137
- SDSS-III Collaboration : Ahn C. P., Alexandroff R., Al-
lende Prieto C., Anderson S. F., Anderton T., An-
drews B. H., Bailey É. A. S., Barnes R., et al. 2012b,
ArXiv:1207.7137
- Seljak U., 1998, *ApJ*, 506, 64
- Seljak U., Hamaus N., Desjacques V., 2009, *Physical Re-
view Letters*, 103, 091303
- Shen Y., Richards G. T., Strauss M. A., Hall P. B.,
Schneider D. P., Snedden S., Bizyaev D., Brewington H.,
Malanushenko V., Malanushenko E., Oravetz D., Pan K.,
Simmons A., 2011, *ApJS*, 194, 45
- Sheth R. K., Rossi G., 2010, *MNRAS*, 403, 2137
- Tegmark M., 1996, *MNRAS*, 280, 299
- Tegmark M., Hamilton A. J. S., Strauss M. A., Vogeley
M. S., Szalay A. S., 1998, *ApJ*, 499, 555
- Tegmark M., Taylor A. N., Heavens A. F., 1997, *ApJ*, 480,
22
- Turner E. L., Ostriker J. P., Gott III J. R., 1984, *ApJ*, 284,
1
- Wetzel A. R., White M., 2010, *MNRAS*, 403, 1072
- White M., Carlstrom J. E., Dragovan M., Holzapfel W. L.,
1999, *ApJ*, 514, 12
- White M., et al., 2012, *MNRAS*, 424, 933
- White M., Hu W., 2000, *ApJ*, 537, 1
- Wolf C., Meisenheimer K., Rix H.-W., Borch A., Dye S.,
Kleinheinrich M., 2003, *A&A*, 401, 73
- Zhang P., Pen U.-L., Bernstein G., 2010, *MNRAS*, 405, 359

APPENDIX A: ESTIMATOR DETAILS

This appendix gives two generalizations of the minimum variance quadratic estimator (Appendix A1), then shows how a prior would impact the estimator (Appendix A2), and finally considers how the estimator and variance change with different basis choices to represent $dN^{(p)}/dz$ (Appendix A3).

A1 Full Estimator

Here we write two more complete expressions for the estimator than were given in the text.

First, the estimator given by Eq. (16) is biased by different cosmic realizations except in the limit in which a large number of modes are used with comparable weight. The full, unbiased estimator replaces Eq. (16) with (Bond et al. 1998,

for more on derivation see ensuing appendix)

$$F_{ij}^{\text{full}} = F_{ij} + \sum_{\ell, m} \text{Tr} \left[\left\{ \begin{pmatrix} \hat{p} \\ \hat{s} \end{pmatrix} \begin{pmatrix} \hat{p} & \hat{s} \end{pmatrix} - \mathbf{A} \right\} \right. \\ \left. \times \left(\mathbf{A}^{-1} \mathbf{A}_{,i} \mathbf{A}^{-1} \mathbf{A}_{,j} \mathbf{A}^{-1} - \frac{1}{2} \mathbf{A}^{-1} \mathbf{A}_{,ij} \mathbf{A}^{-1} \right) \right]. \quad (\text{A1})$$

This expression shows that the estimator is biased by using F_{ij} rather than F_{ij}^{full} at the level of $N_\ell^{-1/2}$, where N_ℓ is the number of modes that contribute. There are $N_\ell = \ell^2_{-2} \sim 10^6 f_{\text{sky}}$ total modes that generally contribute to the estimator (at least when one sample is abundant). Thus, this error will impact the estimator at the $10^{-3} f_{\text{sky}}^{-1/2}$ level. This additional sample variance noise should typically be below the statistical error. We saw no evidence for this bias in the estimates from mock surveys in Section 8.

Secondly, we dropped terms that came from the dependence of A_{00} on the parameter being varied in the Limber approximation estimator presented in the text (eqn. 31). The full estimator in the Limber regime is

$$\hat{N}_k^{(p)} = [\hat{N}_k^{(p)}]_{\text{last}} \\ + [\mathbf{F}^{-1}]_{ki} \sum_{\ell, m} \frac{S[A_{0i}]_{,i}}{A_{00} A_{ii}} \left\{ \left(\delta_{ij}^K + 2 S \frac{A_{0i} A_{0j}}{A_{00} A_{jj}} \right) \hat{p} \hat{s}_j \right. \\ \left. - A_{0d} \left(\frac{\delta_{ij}^K}{A_{dd}} + \frac{S A_{0i} A_{0j}}{A_{00} A_{dd} A_{jj}} \right) \hat{s}_d \hat{s}_j - \frac{S A_{0i}}{A_{00}} \hat{p}^2 - A_{0i} \right\}. \quad (\text{A2})$$

The auto correlation terms that were (as a result of our approximation) omitted in Eq. (31) become important when $\sum_i A_{0i}^2/[A_{00} A_{ii}] \sim 1$. We found that their effect was most evident when considering photo- z calibration.

A2 Impact of Prior

The estimator given in Eq. (16) follows from using the multi-dimensional Newton's method to find the zeros of the derivative of the log of the data Likelihood function, $\log \mathcal{L}$ (Bond et al. 1998):²²

$$\hat{N}_i = [\hat{N}_i]_{\text{last}} - ([\log \mathcal{L}]_{,,})_{ij}^{-1} [\log \mathcal{L}]_{,j}, \quad (\text{A3})$$

where $[\log \mathcal{L}]_{,,}$ is the Hessian of $\log \mathcal{L}$, which upon ensemble average is the negative of the Fisher matrix. For a Gaussian Likelihood with covariance matrix \mathbf{C} and data vector Δ , $[\log \mathcal{L}]_{,i} = \Delta^T \mathbf{C}^{-1} \mathbf{C}_{,i} \mathbf{C}^{-1} \Delta / 2$.

With this derivation in mind, it is straightforward to generalize Eq. A3 to include a prior:

$$\hat{N}_i = [\hat{N}_i]_{\text{last}} - ([\log \mathcal{L}]_{,,} + [\log \mathcal{L}_P]_{,,})_{ij}^{-1} ([\log \mathcal{L}]_{,j} + [\log \mathcal{L}_P]_{,j}), \quad (\text{A4})$$

where \mathcal{L}_P is the prior likelihood function. The case of a Gaussian prior on the N_i is given by Eq. (64).

As an application of the above, let us consider the case of our $N_i^{(p)}$ estimator in which the $b_i^{(s)}$ are imperfectly known and instead are constrained by prior information. Remember that since the $N_i^{(p)}$ are estimated from cross-correlations, they are completely degenerate with $b_i^{(s)}$ and can only be

²² Newton's method is applied to the log of the likelihood rather than the likelihood itself because Newton's method provides exact estimates for the extrema of a quadratic function.

separated with a prior from the auto-correlation measurements. In this case, the Fisher matrix of the parameters $N_i^{(p)}$ and $b_i^{(s)}$ plus a prior on $b_i^{(s)}$ yields the new error matrix:

$$\mathbf{F}^{bs} = \frac{F_{ii}^S}{[N_i^{(p)}]^2} \begin{pmatrix} [N_i^{(p)}]^2 & N_i^{(p)} b_i^{(s)} \\ N_i^{(p)} b_i^{(s)} & [b_i^{(s)}]^2 \end{pmatrix} + \begin{pmatrix} 0 & 0 \\ 0 & \sigma_{bs}^{-2} \end{pmatrix}, \quad (\text{A5})$$

where σ_{bs} is the standard deviation of the Gaussian prior on $b_i^{(s)}$ centered on $[b_i^{(s)}]_{\text{prior}}$. Our previous results correspond to $\sigma_{bs} \rightarrow 0$. (We are ignoring redshift-bin correlations in the prior for simplicity, but such correlations can be easily incorporated.) The fractional variance on a measurement of $N_i^{(p)}$ is thus

$$\left(\frac{\delta N_i^{(p)}}{N_i^{(p)}} \right)^2 \equiv [\mathbf{F}^{bs}]_{ii}^{-1} = [F_{ii}^S]^{-1} \left(1 + \left[\frac{N_i^{(p)} \sigma_{bs}}{b_i^{(s)}} \right]^2 F_{ii}^S \right). \quad (\text{A6})$$

Therefore, the fractional variance in the estimated $b_i^{(s)}$ is the limiting factor when it is larger than the fractional variance in the estimate of $N_i^{(p)}$ for the case that $b_i^{(s)}$ is held fixed.

The estimator in this limit is

$$\begin{aligned} \hat{N}_i^{(p)} &= [\hat{N}_i^{(p)}]_{\text{last}} + \frac{1}{F_{ii}^S} \sum_{\ell, m} \frac{[A_{0i}]_{\ell, i}}{A_{00} A_{ii}} \{ \hat{p} \hat{s}_i - A_{0i} \} \\ &+ N_i^{(p)} \left([b_i^{(s)}]_{\text{prior}} / [\hat{b}_i^{(s)}]_{\text{last}} - 1 \right). \end{aligned} \quad (\text{A7})$$

with the complementary estimator for the bias being trivially $\hat{b}_i^{(s)} = [b_i^{(s)}]_{\text{prior}}$.

For the case of SDSS or BOSS quasars (where $N^{(s)} \sim 10^5$), the variance in the measured bias is $\sigma_{bs} \sim 0.1$ (Ross et al. 2009; White et al. 2012), which is comparable to the redshift error expected from cross-correlations (Fig. 7). However, for rare samples with fewer spectra than SDSS quasars, the uncertainty in σ_{bs} will dominate the error in the $N_i^{(p)}$.

A3 Estimator and constraints in other bases

We have chosen a top hat basis set for convenience, which also leads to an estimator that converges robustly to the peak. Other choices are clearly possible, and they may be preferred in some situations. For example, instead of $N_i^{(p)}$ we could estimate the parameters of a particular functional form. Or we could expand $dN^{(p)}/dz$ as a sum of overlapping Gaussians or (orthogonal) polynomials times basis functions (e.g. a power law times an exponential). While the quadratic estimator formalism is completely general, it is not trivial to recast the estimator in terms of an arbitrary basis set as **A** needs to be recast in terms of the new parameter set. In many cases, this is not analytically expressible (with an exception being the linear case we discuss below). However, it is trivial to translate our results for the error on a parameter into another basis set. The new Fisher matrix is given by the chain rule:

$$\mathbf{F}' = \mathbf{W}^T \mathbf{F} \mathbf{W}, \quad (\text{A8})$$

where \mathbf{W} is the Jacobian matrix between the $N_i^{(p)}$ and the new parameter set λ_i . We showed that the Fisher matrix is often well approximated as diagonal, such as in the Schur-Limber limit. In this case

$$F'_{ij} \approx \sum_{k=1}^{N_{\text{bin}}} \frac{1}{F_{kk}^S} \frac{dN_k^{(p)}}{d\lambda_i} \frac{dN_k^{(p)}}{d\lambda_j}. \quad (\text{A9})$$

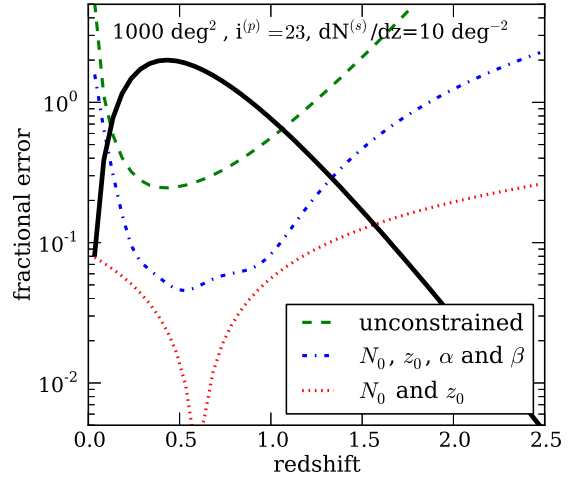


Figure A1. Improvement in constraints from a constrained parametrization of $dN^{(p)}/dz$ rather than the case considered in the text in which the $N_i^{(p)}$ are free. Shown are surveys with the parameters $i^{(p)} = 23$, $dN^{(s)}/dz = 10 \text{ deg}^{-2}$, and $\Delta z = 0.05$ over $1,000 \text{ deg}^2$ and $0 < z < 2.5$. The fractional errors for the unconstrained case – the case investigated in the body of this paper – are given by the green dashed curve, and the case where $b^{(p)} dN^{(p)}/dz$ is constrained by the functional form $N_0 (z/z_0)^\alpha \exp[-(z/z_0)^\beta]$, marginalizing over the parameters specified in the key, is given by the dot-dashed blue and dotted red curves. This constraining functional is evaluated at the fiducial parameters given by Eq. (3) for these two cases. The black solid curve shows $dN^{(p)}/dz$, arbitrarily normalized.

Once the $N_i^{(p)}$ are estimated with our technique, they can be combined to estimate the λ_i with error given by \mathbf{F}' .

Fig. A1 shows an example using Eq. A8 in which we changed basis to one in which $dN^{(p)}/dz$ is constrained to have the smooth functional form specified in the key (a generalization of our Eq. (3) for $P(z, i)$). This figure investigates the case of a photometric population with $i^{(p)} = 23$ and with a low density of spectroscopic objects given by $dN^{(s)}/dz = 10 \text{ deg}^{-2}$, overlapping over a sky area of $1,000 \text{ deg}^2$ (although, the total number of spectra, here 10^4 , is the essential quantity). It shows that the constraints are substantially improved even if a fairly general functional form is assumed (varying 2 parameters for the dotted curves and 4 for the dot dashed). One advantage of parametrizing $dN^{(p)}/dz$ with a smooth functional form is that the constraints do not depend on the choice of Δz .

Finally, we note that the formalism this paper developed for estimating the $N_i^{(p)}$ can be trivially recast for models in which one instead aims to constrain some set of basis functions ϕ_i for which $dN^{(p)}/dz = \sum_i c_i \phi_i(z)$, where c_i are a set of coefficients. In this case, the primary difference is that for the $\alpha_\ell(k, z_i)$ that went into calculating $\mathbf{C}(\ell)$, the index i no longer indexes the redshift bin but rather the basis function.

APPENDIX B: EXTENDED LIMBER APPROXIMATION

The Limber approximation is most applicable on small angular scales, where we may approximate the sky as flat and the spherical harmonic transform as a Fourier transform (e.g. White et al. 1999; Pápai & Szapudi 2008). With these approximations, the angular correlation function can be written as

$$w(\theta) = \int d\chi_1 d\chi_2 W(\chi_1)W(\chi_2) \times \int \frac{d^3k}{(2\pi)^3} P(k) e^{i\mathbf{k} \cdot (\mathbf{x}_1 - \mathbf{x}_2)}, \quad (\text{B1})$$

$$\approx \int \frac{d^3k}{(2\pi)^3} P(\mathbf{k}_\perp, k_\parallel) \int d\bar{\chi} W^2(\bar{\chi}) e^{i\mathbf{k}_\perp \cdot \bar{\mathbf{x}}_\perp} \times \int dZ e^{ik_\parallel Z}, \quad (\text{B2})$$

$$= \int \frac{K_\perp dK_\perp}{2\pi} P(\mathbf{k}_\perp, k_\parallel = 0) \times \int d\bar{\chi} W^2(\bar{\chi}) J_0(k_\perp \bar{\chi}), \quad (\text{B3})$$

where in the second line we have changed variables from χ_i to center-of-mass and relative coordinates, $\bar{\chi} = (\chi_1 + \chi_2)/2$ and $Z = \chi_1 - \chi_2$, and assumed W is so broad that $W(\bar{\chi} \pm Z/2) \approx W(\bar{\chi})$ (which is not always the case for the W considered in the text). Writing $\ell = k_\perp \bar{\chi}$ and using $J_0(\ell\theta) \simeq P_\ell(\cos\theta)$ for $\theta \ll 1$ and $\ell \gg 1$, the angular power spectrum, C_ℓ , is thus

$$C_\ell = \int d\chi \frac{W^2(\chi)}{\chi^2} P(k_\perp = \ell/\chi, k_\parallel = 0). \quad (\text{B4})$$

The Limber approximation further results in correlations between non-overlapping redshift slices being zero.

One can compare the Limber approximation to the analytic solution for certain cases to see when and how well these approximations work. Let us assume $W(\chi)$ is a top-hat in χ in slices of width $\Delta\chi$ (as in the main body of this paper). Then, the cross-spectrum is

$$\ell^2 C_{ij} = k_\perp^2 \int \frac{dk_\parallel}{2\pi} e^{ik_\parallel(\chi_i - \chi_j)} \text{sinc}\left[\frac{k_\parallel \Delta\chi}{2}\right]^2 P(k_\perp, k_\parallel). \quad (\text{B5})$$

Using the method of steepest descents (or approximating the power spectrum as a power-law and using the asymptotic behavior of the resulting Bessel functions), it can be shown that for $k_\perp |\chi_i - \chi_j| \gg 1$

$$\ell^2 C_{ij} \rightarrow \ell^2 C_{ij}^{\text{asympt}} \equiv \frac{k_\perp}{\Delta\chi^2} P(k_\perp) e^{-k_\perp |\chi_i - \chi_j|}, \quad (\text{B6})$$

We can make further progress by assuming that $P(k)$ is a power-law. In particular, if $P(k)$ is a power-law with index -2 , roughly the index on galaxy scales in our Universe, the integral in Eq. B5 has simple poles that make the evaluation trivial:

$$\ell^2 C_{ij} = \ell^2 C_{ij}^{\text{asympt}} \begin{cases} k_\perp \Delta\chi + \exp[-k_\perp \Delta\chi] - 1 & i = j; \\ \cosh[k_\perp \Delta\chi] - 1 & i \neq j. \end{cases} \quad (\text{B7})$$

Note that when $i = j$ and $k_\perp \Delta\chi \gg 1$ we recover the Limber result $\ell^2 C_{ii} \simeq (k_\perp^2 / \Delta\chi) P(k_\perp)$. In addition, at $k_\perp \Delta\chi = 2$, Eq. B7 undershoots Limber by 40 per cent with this percentage decreasing roughly linearly with increasing $k_\perp \Delta\chi$. The

errors from Limber will be smaller when $P(k)$ has a flatter power-law, as is the case at $k_\perp \Delta\chi \sim 1$ for the $\Delta\chi$ considered in the text. That the Limber approximation works so well once $k_\perp \Delta\chi$ moderately exceeds unity helps explain why in the text we find it to be such a good approximation for our problem. Similarly, for $P(k)$ equal to a constant Eq. B5 can also be evaluated, yielding $C_{ij} = C_{ii}^{\text{asympt}} k_\perp \Delta\chi \delta_{ij}^K$. This is exactly the Limber result, which is not surprising as the constant term is what is maintained in the Limber approximation.

Next, consider the impact of redshift-space distortions (RSDs) in the Limber approximation, which have been neglected in all of our prior discussion. RSDs could be interesting for our purposes because they break the $b_i^{(x)} - N_i^{(x)}$ degeneracy. On linear scales the lowest-order correction owing to RSDs is to multiply the power spectrum by $1 + 2\beta_i \mu^2$, where $\mu = k_\parallel / k$ and $\beta_i \simeq \Omega_m^{0.6} / b_i^{(x)}$, with the redefinition of χ and \mathbf{k} to be the analogous redshift-space quantities (Kaiser 1987; Hamilton 1992). In the Limber approximation, $|k_\parallel| \lesssim \Delta\chi^{-1}$ and so we expect $|\mu| \ll 1$ and the correction to be small. However, how quickly this falls off depends on $W(\chi)$. In the case of our top hat window function and with the replacement $P(k_\perp, k_\parallel) \rightarrow P(k_\perp)(1 + 2\beta_i \mu^2)$ – which is analogous to the Limber approximation –, Eq. B5 can be integrated analytically yielding

$$\ell^2 C_{ii} = \frac{k_\perp^2}{\Delta\chi} P(k_\perp) \left(1 + \frac{2\beta_i}{k_\perp \Delta\chi}\right), \quad (\text{B8})$$

and with the off-diagonals being zero. Thus, the RSD correction falls off slowly as $(k_\perp \Delta\chi)^{-1}$ in the case of top hat W . A curiosity is that if we had approximated μ as k_\parallel / k_\perp , the integral would have diverged. Thus, in the case of a top hat W the RSD term arises from modes with $\mu \sim 1$.

However, smoother $W(\chi)$ result in RSDs having a weaker scaling in the Limber regime. Consider the case in which $W(\chi)$ is a Gaussian with standard deviation σ . The analogous equation to Eq. B5 for this case is

$$\ell^2 C_{ij} = k_\perp^2 \int \frac{dk_\parallel}{2\pi} e^{ik_\parallel(\chi_i - \chi_j)} \exp[-k_\parallel^2 \sigma^2] P(k_\perp, k_\parallel). \quad (\text{B9})$$

For large σ the integral is dominated by small k_\parallel , and we can Taylor series expand about $k_\parallel = 0$ as above. In this case, the correction due to redshift-space distortions enters at order $\mathcal{O}([k_\perp \sigma]^{-2})$. The RSD term is similar (merely increasing by a factor of 2) if one of the two window functions were much narrower than σ . In addition, exponential or triangle window functions also have RSDs entering at $\mathcal{O}([k_\perp \sigma]^{-2})$.²³

It is important for our calculations if the RSDs in Limber contribute at $\mathcal{O}([k_\perp \sigma]^{-1})$ rather than $\mathcal{O}([k_\perp \sigma]^{-2})$, where σ is the width of our window function. RSDs would be a promising signal to break the $b_i^{(x)} - N_i^{(x)}$ degeneracy if the former scaling held, but are not in the case of the latter. It may appear with the formalism in the text, which uses top hat W_i , that the $\mathcal{O}([k_\perp \sigma]^{-1})$ scaling would apply. However,

²³ This result that RSDs depend on the smoothness of $W(\chi)$ is analogous to the finding in Nock et al. (2010). There, the impact of RSDs on the correlation function measured in a top hat projection over ~ 100 Mpc was shown to be much more significant than when the effective window was smoothed with a pair-averaging scheme.

for the case of interest where the $dN^{(p)}/dz$ is a smooth function that is not known, we posit that one is always in the regime where the RSD term falls off as $\mathcal{O}([k_\perp \sigma]^{-2})$. Basis functions can always be chosen that have smooth $W(\chi)$ and where the RSD terms contribute at $\mathcal{O}([k_\perp \sigma]^{-2})$. That they contribute at $\mathcal{O}([k_\perp \sigma]^{-1})$ for top hat windows is a pathological result of our basis choice that implicitly assumes that the distribution of $dN^{(p)}/dz$ is a histogram with sharp breaks between redshift steps. Thus, to include RSDs properly requires a smoother basis set for the W_i than we take in the text. Because of this added complication, we do not consider RSDs in our formulae in the text. For the reasons espoused above and because the modes that contribute to our estimate are generally safely in the Limber regime, the bias from ignoring them should be small.

APPENDIX C: MAGNIFICATION BIAS

C1 Effect of magnification

The spatial density of observed galaxies is modulated by an additional factor that we have ignored so far of $(1+\delta_\mu)$ owing to lensing magnification (Turner et al. 1984; Fugmann 1988; Narayan 1989; Hui et al. 2007, 2008). In the weak lensing regime,

$$\delta_\mu(\hat{\mathbf{n}}, z_i) \equiv 2(-\alpha_i^{(x)} - 1) \int_0^{\chi_i} d\chi \frac{\chi_i - \chi}{\chi_i} \chi \nabla_\perp^2 \phi(\chi, \hat{\mathbf{n}}), \quad (\text{C1})$$

where ∇_\perp^2 is the comoving Laplacian in the plane perpendicular to the radial direction and $\alpha_i^{(x)}$ is the power-law slope of the cumulative number of sources at the survey flux threshold and redshift z_i . (Note that $\alpha_i^{(x)}$ is defined to be a negative number as long as the cumulative number decreases with increasing flux.) Thus, magnification generates additional correlations such that

$$C_{ij} \rightarrow C_{ij} + C_{ij}^{\delta\mu} + C_{ji}^{\delta\mu}, \quad (\text{C2})$$

where $C_{ji}^{\delta\mu}$ is the cross-correlation function between the galaxy overdensity field in redshift slice j and $\delta_{\mu,i}$, and we are dropping the smaller $C_{ij}^{\mu\mu}$ term. In the Limber regime, the expression for the new terms in Eq. C2 is (Bartelmann & Schneider 2001, their Eq. 7.9)

$$C_{ij}^{\delta\mu} = - \left(\frac{\alpha_i^{(x)} + 1}{b_i^{(x)}} \right) \frac{3H_0^2 \Omega_0}{c^2} \int \frac{d\chi}{\chi a} W_j(\chi) Y_i(\chi) D^2(\chi) P\left(\frac{\ell}{\chi}\right), \quad (\text{C3})$$

for $i > j$. Otherwise, $C_{ij}^{\delta\mu} = 0$ (we set this to zero for $i = j$ in our calculations), and we denote the source population in question by x and lens by y as it could be either the photometric or spectroscopic sample. Here,

$$Y_i(\chi) = \int_\chi^\infty d\chi' W_i(\chi') \frac{\chi' - \chi}{\chi'}. \quad (\text{C4})$$

Magnification depends only on the bias of the lens and not the source and so can break the degeneracy between bias and number. (This dependence may be opaque in our notation as the $C_{ij}^{\delta\mu}$ enter \mathbf{A} multiplied by factors of the bias.)

Noting that $c^2/(3H_0^2 \Omega_m) = 2 \times 10^7 \text{ Mpc}^2$, a back-of-

the-envelope estimate for $C_{ij}^{\delta\mu}$ is

$$C_{ij}^{\delta\mu} \approx - \left(\frac{\alpha_i^{(x)} + 1}{b_i^{(x)}} \right) \frac{(1+z_j) D^2(z_j) P\left(\frac{\ell}{\chi_j}\right)}{(2 \times 10^7 \text{ Mpc}^2)} \left(\frac{1}{\chi_j} - \frac{1}{\chi_i} \right) \quad (\text{C5})$$

when $i > j$, and we have approximated W_i and W_j as sharply peaked around their respective redshifts. This is similar to the C_{jj} term without lensing (Eq. 21), differing most importantly by the factor $[(1+z_j) \chi_j \Delta \chi_j]/2 \times 10^7 \text{ Mpc}^2$. This factor is $\mathcal{O}(10^{-2})$ for populations at $z \sim 1$ and $N_{\text{bin}} \sim 50$, but can be larger for higher redshift populations. Thus, magnification will add off-diagonal terms that are $\mathcal{O}(10^{-2})$ of the diagonal terms in \mathbf{C} and were zero in our previous treatment. (\mathbf{C} was typically approximated as diagonal in the text.) The new magnification terms have a larger impact on the components in \mathbf{A} involving p , as these terms sum over i and j in C_{ij}

C2 Photo- z calibration with magnification

Here we discuss how magnification could potentially be corrected in the application of photo- z calibration investigated in Section 7.1 (and we use the same notation as introduced there). We consider a simplified problem in which most of the pm photo- z sample is concentrated at redshift z_m . Then, there is a significant bias if the error on $T_i^{(pm)}/T_m^{(pm)}$ is comparable to $C_{mi}^{\delta\mu}/C_{ii}$, which we just showed is $\mathcal{O}([N_{\text{bin}}]^{-1})$ for $z_i \sim 1$, where the number of bins here is set by how broad the bins have to be for a single bin to encompass most of pm .

The minimum variance estimator with a prior on the $\alpha_i^{(x)}$ (which enters analogously to the number prior in Eq. 64) can also be written for this simplified problem: First, the covariance matrix at some ℓ and in the Limber approximation is

$$D_{00} \approx [T_m^{(pm)}]^2 C_{mm} + w^{(pm)} + \mathcal{M}, \quad (\text{C6})$$

$$D_{01} \approx T_j^{(pm)} T_j^{(s)} C_{jj} + T_m^{(pm)} T_j^{(s)} C_{mj}^{\delta\mu} + w_j^{(pms)}, \quad (\text{C7})$$

$$D_{11} \approx [T_j^{(s)}]^2 C_{jj} + w_j^{(s)}, \quad (\text{C8})$$

where \mathcal{M} encompasses the impact of all magnification on the photometric sample, and we have dropped terms that do not contain $T_m^{(pm)}$ except the off-diagonal dependence of $T_i^{(pm)}$. For the specified \mathbf{D} and a prior on $\alpha^{(x)}$ with variance σ_α , the minimum variance quadratic estimator is

$$\widehat{T_i^{(pm)}} = \widehat{[T_i^{(pm)}]_{\text{last}}} + [\mathbf{F}^{-1}]_{11} \sum_{\ell, m} \frac{S' T_j^{(s)} C_{ij}}{D_{00} D_{11}} (\widehat{p_m} \widehat{s_i} - D_{01}), \quad (\text{C9})$$

where $S' = D_{00} D_{11} (D_{00} D_{11} + D_{01}^2) / \det[\mathbf{D}]^2$, $\alpha^{(x)}$ is set by the prior, we have assumed that $T_m^{(pm)}$ is well constrained by other cross (and auto) correlations (which is quite likely), and \mathbf{F} also has a simple analytic representation. This estimator is quite analogous to our previous estimator.

It is instructive to look at the variance on a measurement of $T_i^{(pm)}$ in a single mode:

$$[\mathbf{F}^{-1}]_{11} = \frac{D_{00} D_{11} + S' [T_m^{(pm)} T_j^{(s)} C_{mj}^{\delta\mu} / (\alpha + 1)]^2 \sigma_\alpha^2}{(S' T_j^{(s)} C_{ij})^2}. \quad (\text{C10})$$

This equation shows that error on the magnification bias

times S' (the latter term in the numerator) has to be comparable to the auto power terms (the former term) in order to change our previously quoted errors in Section 7.1. It also suggests that it may be desirable to down weight large-angle modes where S' is largest (that have the smallest noise) and, hence, where the fog from lensing is most disruptive.

APPENDIX D: RECURRENCE RELATIONS FOR (AND THE EVALUATION OF INTEGRALS OVER) SPHERICAL BESSEL FUNCTIONS

Throughout we need to perform integrals over spherical Bessel functions. Numerical methods for evaluating spherical Bessel functions and integrating over them are well advanced, but do not seem to be widely known. This appendix gives the details of the algorithms used in this study. Further details can be found in (Miller 1952; Corbató & Uretsky 1959; Gillman & Fiebig 1988; Poularikas 2000) or at <http://www.utdallas.edu/~cantrell/ee6481/lectures/bessres1.pdf>.

First we address the evaluation of the j_ℓ . For small values of the argument, we use a series expansion of $j_\ell(x)$. For larger values, we evaluate the j_ℓ using a downwardly stable recurrence relation for $r_\ell \equiv j_\ell/j_{\ell-1}$. Specifically we first initialize r_L by setting $j_L(x) = 0$ for L much larger than any ℓ of interest (and x). Then the relation

$$r_{\ell-1} = \frac{1}{(2\ell-1)/x - r_\ell} \quad (\text{D1})$$

is downwardly stable and can be used to find r_ℓ for $0 < \ell < L$. The j_ℓ can then be evaluated by moving up the hierarchy after initializing $j_0(x) = \sin(x)/x$.

Eqs. (13) and (14) are difficult integrals to evaluate owing to the oscillatory nature of the j_ℓ . We experimented with using the scheme suggested in Lucas (1995) of decomposing the product of j_ℓ into a sum of functions that each have a single oscillatory period at large arguments and then using the transformations discussed therein on a series where the n^{th} member is our k -integral evaluated from 0 out to the n^{th} zero. This operation removes oscillatory behavior in this slowly converging series so that it converges more quickly to the $n \rightarrow \infty$ limit, and the integral converges for $n \sim 10$ (Lucas 1995). Experiments with some of the integral terms indicated that the Lucas (1995) method was much faster than a brute-force integration, but we were able to find a simpler implementation which was sufficiently fast and accurate. In particular, we ended up evaluating these integrals by brute force, integrating typically out to the 1,000th zero of the $\alpha_\ell(k, z_i)$ (which were pre-computed and stored in a table). A slight improvement in the convergence of the integral was obtained by applying a Gaussian damping to the integrand – based on the fact that $k_\parallel \gg \ell/\chi$ should not contribute much to the integral. The details of this damping did not affect our results.

APPENDIX E: THE POWER-LAW CASE

It is of interest to work through the expressions for the angular power spectrum and correlation function within the Limber approximation (depth of survey \gg length scales of

interest) and assuming that the underlying power spectrum is a power-law.

Recall that within the Limber approximation (Section 3.1)

$$C_\ell = \int d\chi P(k) \frac{W^2(\chi)}{\chi^2}, \quad (\text{E1})$$

where $W(\chi)$ is the projection kernel that defines the 2D (projected) overdensity in terms of the 3D, and it integrates to unity against $d\chi$. We shall assume that $W(\chi)$ is peaked at χ_0 and of width $\Delta\chi$ such that $k\chi_0 \gg k\Delta\chi \gg 1$ for scales, k , which contribute significantly.

Assuming a power-law power spectrum of the form $\Delta^2(k) \equiv k^3 P(k)/2\pi^2 = (k/k_\star)^{3+n}$, with $-2 < n < -1$, the real-space 3D correlation function is

$$\xi(r) = \left(\frac{r_0}{r}\right)^\gamma = \int \frac{dk}{k} \Delta^2(k) j_0(kr) = B_n (k_\star r)^{-3-n}, \quad (\text{E2})$$

where $B_n \equiv -\sin(n\pi/2) \Gamma(2+n, 0)$, which respectively equals 1.25 and 1 for $n = -3/2$ and $n = -1$ (B_n diverges as $n \rightarrow -3^+$). It follows from Eq. E2 that $\gamma = n+3$ and $r_0 = B_n^{1/\gamma}/k_\star$.

In the Limber approximation,

$$C_\ell = \frac{2\pi^2}{k_\star^3 \mathcal{V}} \left(\frac{\ell}{k_\star \chi_0}\right)^n, \quad (\text{E3})$$

where $\mathcal{V} = \chi_0^2 \Delta\chi$ is the volume per steradian. Using analogous relations to Eq. E2, the 2D or projected correlation function is

$$w(\theta) = \left(\frac{\theta_\star}{\theta}\right)^{n+2} = \frac{\pi A_n}{k_\star^3 \mathcal{V}} (k_\star \chi_0)^{-n} \theta^{-n-2}, \quad (\text{E4})$$

where $A_n \equiv 2^{n+1} \Gamma(1+n/2)/\Gamma(-n/2) \simeq 2.1$ and 1 for $n = -3/2$ and $n = -1$ (A_n diverges as $n \rightarrow -2^+$).

Particularly simple expressions hold in the case $n = -1$ for which $A_n = B_n = 1$, so $\Delta^2 = (k/k_\star)^2$

$$\xi(r) = \left(\frac{r_0}{r}\right)^2 \quad \text{where} \quad r_0 = k_\star^{-1}, \quad (\text{E5})$$

and

$$w(\theta) = \left(\frac{\theta_\star}{\theta}\right) = \pi \left(\frac{r_0}{\chi_0}\right)^2 \left(\frac{\chi_0}{\Delta\chi}\right) \theta^{-1}. \quad (\text{E6})$$